Damage Survey, Radar, and Environment Analyses on the First-Ever Documented Tornado in Beijing during the Heavy Rainfall Event of 21 July 2012

ZHIYONG MENG AND DAN YAO

Laboratory for Climate and Ocean–Atmosphere Studies, Department of Atmospheric and Oceanic Sciences, School of Physics, Peking University, Beijing, China

(Manuscript received 7 May 2013, in final form 21 March 2014)

ABSTRACT

On 21 July 2012, severe wind damage occurred in Beijing, China, during a heavy rainfall event. Through a damage survey that had the most detailed information in all of the published tornado damage surveys so far in China, this work showed significant evidence that the wind damage was caused by a mesocyclonic tornado rated as a category 3 storm on the enhanced Fujita scale (EF3) that was observed by people but of which not a single picture was taken. This was the first tornado ever reported or documented in Beijing. The most influential evidence indicating a tornado included a narrow damage swath 30–400 m wide and ~10 km long and convergent surface winds at multiple places along the swath. The radar analyses examined here show that the tornado was embedded in a strong mesocyclone. The initial linear and later sinusoidal tornado track was likely due to the intensification and expansion of the mesocyclone. The location, timing, and intensity variation of the wind damage were precisely collocated with those of a tornadic vortex signature. Descending reflectivity cores as well as their associated jetlets and counterrotating vortices were detected both before tornadogenesis and prior to the reintensification of the tornado damage. A tornadic debris signature was also detected in the later stages of the tornado. Compared to the U.S. climatology of forecast parameters for different storm categories, this storm developed in an environment that was favorable for the formation of supercells or weakly tornadic supercells rather than significantly tornadic supercells.

1. Introduction

On 21 July 2012, an extremely severe rainfall event took place in Beijing, China. An average 24-h precipitation amount of 190 mm in the urban area and a maximum of 460 mm of precipitation in the suburban area were observed, and 78 people were killed (Chen et al. 2012). In addition to floods, severe wind damage occurred in the town of Zhangjiawan (Fig. 1a) in the southeastern part of the metropolitan area of Beijing (Fig. 1b, black boundary; hereafter, when ''Beijing'' is referred to, it means this metropolitan area, unless otherwise specified). The wind damage started at ~1340 local standard time (LST, which is UTC + 8 h) 21 July, lasting for ~20 min, and having a path ~10 km long. Seven villages were affected including Houtuo (HT), Dabeiguan (DBG), Xiaobeiguan (XBG), Fatou (FT), Zaolinzhuang (ZLZ), Daxinzhuang (DXZ), and Xidingfuzhuang (XDFZ) (Fig. 1a). Two people were killed in ZLZ. A number of trees were either uprooted or snapped along the damage path. A question to ask is what kind of weather system caused the damaging winds.

Following the pioneering work of Theodore Fujita (Fujita 1981), damage surveys have been widely performed in the United States to infer tornado wind features (e.g., Davies-Jones et al. 1978; Bluestein et al. 1997; Marshall 2002; Speheger et al. 2002; Wakimoto et al. 2003). If there is no photographic evidence of funnel clouds, a damage survey would be the only way to discriminate a tornado from other wind phenomena. Two phenomena are typically responsible for causing severe wind damage: tornadoes and downbursts (or quasi-straight-line winds). Doswell (2003) described the differences in the direction of scattered debris between a tornado and a downburst (Fig. 2). The most significant features of the damage pattern caused by a tornado are a narrow damage swath and convergent surface debris

Corresponding author address: Dr. Zhiyong Meng, Laboratory for Climate and Ocean–Atmosphere Studies, Dept. of Atmospheric and Oceanic Sciences, School of Physics, Peking University, 209 Chengfu Road, Beijing 100871, China.
E-mail: zymeng@pku.edu.cn

DOI: 10.1175/WAF-D-13-00052.1

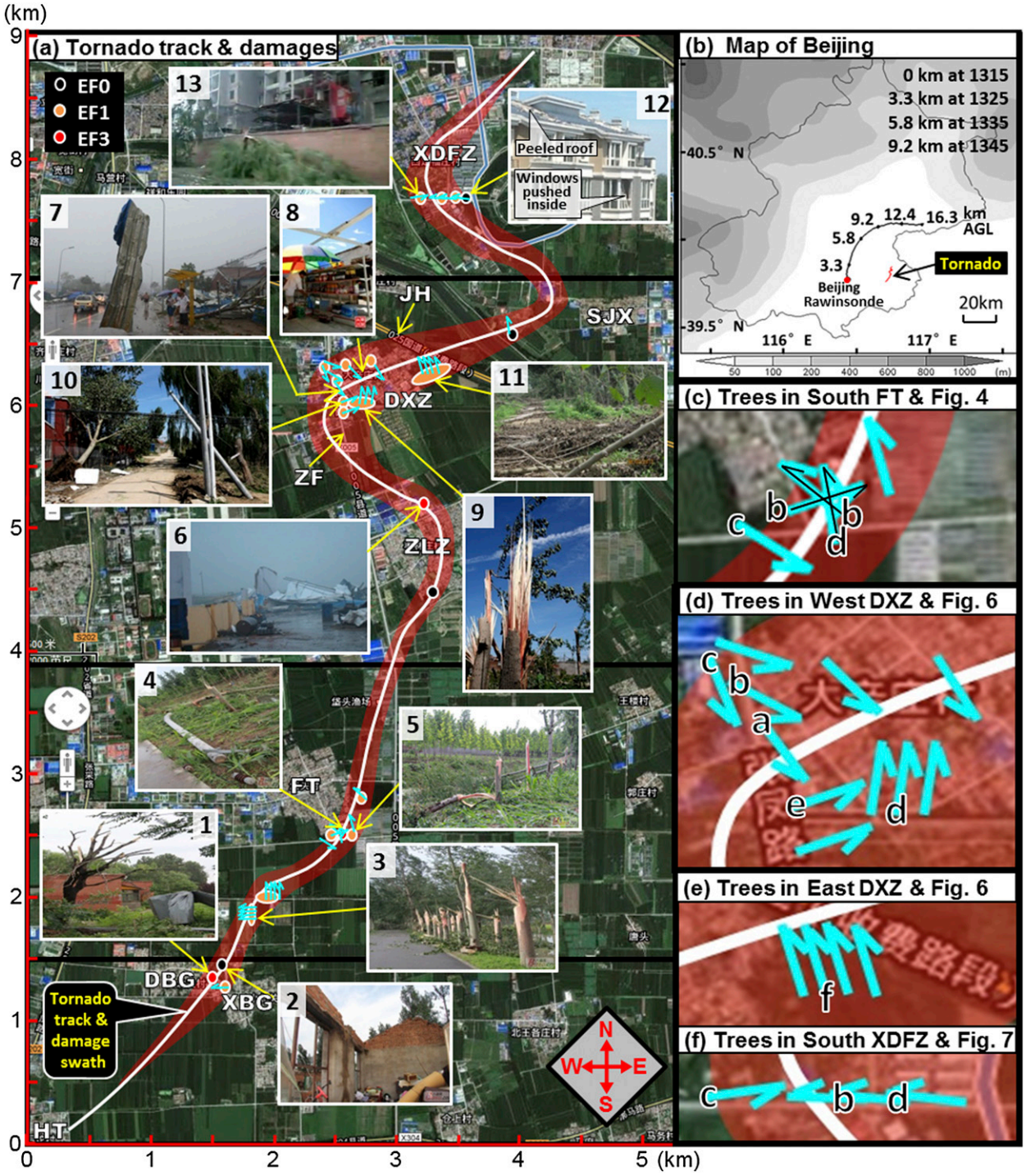

FIG. 1. (a) The tornado track (white line) and damage swath (red shading) on a satellite map obtained from Google Earth with some damage pictures at DBG (1 and 2), XBG (3), FT (4 and 5), ZLZ (6), DXZ (7–11), and XDFZ (12 and 13). Pictures 1–5 were provided by Bato.cn, 6 and 7 by 591hx.com, 8–10 by M. Zhang, 12 by Sina.com.cn, and 13 by Youku.com. The small light-blue arrows denote the direction of tree fall. The colored dots denote the EF scale of the damage. The direction of the map is given in the bottom-right corner. (b) The tornado track (red line) on a map of Beijing with terrain height (shaded), the rawinsonde and radar station (the same location as the red dot) of Beijing, and the height (km AGL) and time variation of the air balloon of the rawinsonde at 1400 LST. The map scale in (b) is given in its bottom-right corner. Shown are enlargements of (a) for the fallen trees at (c) south FT, (d) west DXZ, (e) east DXZ, and (f) south XDFZ. The photograph of the trees indicated by lowercase letters in (c)–(f) (placed at the end of the denoted arrow) are shown in Figs. 4, 6, 6, and 7, respectively, labeled with the same lowercase letters.

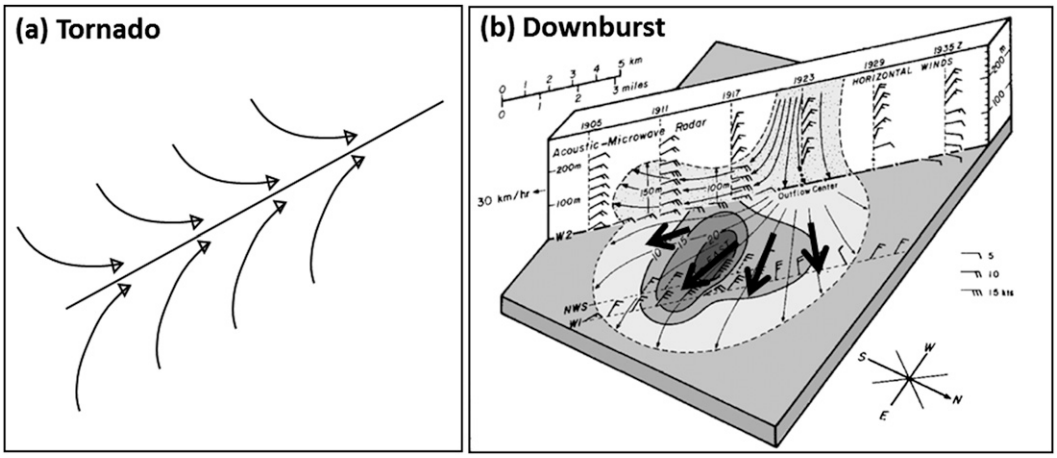

FIG. 2. Schematics of surface wind in a (a) tornado [adapted from Doswell (2003)] and a (b) downburst [adapted from Markowski and Richardson (2010)].

(Fig. 2a; Doswell 2003), while straight-line winds tend to cause short and broad fan-shaped diverging surface debris patterns (Fig. 2b; Bunting and Smith 1993; Doswell 2003; Markowski and Richardson 2010). Doswell (2003) reported that surface converging wind is a more important indicator of a tornado than is direct evidence of rotation, and the closer to the ground, the greater the predominance of the convergent over the rotational flow.

What caused the wind damage in southeastern Beijing on 21 July 2012 has been difficult to determine. First of all, tornadoes have never been reported in Beijing. Tornadoes in China occur mainly along the lower reaches of the Yellow River (around 35°N, 115°E) (Zhao 1995) similar to the high frequency location of squall lines (Meng et al. 2013). Second of all, some witnesses saw a funnel cloud, but no one took a single photograph of the tornado. Third of all, no professional observation of the tornado was obtained. The only way to determine whether a tornado occurred was through conducting a damage survey. The objective of this work was to determine whether the wind damage was caused by a tornado based on damage surveys as well as radar and environment analyses.

Likely due to the low frequency of tornadoes in China, only a few damage surveys in China have been documented in the literature. Those that have been were typically too brief due to a lack of detailed evidence. Most of damage surveys have been just a brief list of the timing and location, a rough diameter of the damage swath, the number of fatalities, damaged buildings and trees, etc. (e.g., Fang et al. 2009), as well as a qualitative description of the severe destruction at one or two places. Those surveys have mainly focused on limited aspects; thus, they were not quite comprehensive. For example, based on a damage survey of a tornado that occurred in 1977 in Hubei Province, Yang et al. (1978) described the shape and color of the funnel cloud, the sound of the tornado, water that was sucked up and out of a pond, and the rotation indicated by tree fall. They, however, did not provide a single photograph of the described features. Lin (1995) focused on describing the destruction at some spots caused by a tornado associated with a severe tropical storm in 1994 in Guangdong Province. Although the paper showed two photographs of a damaged vehicle and a metal panel wrapped around a telephone pole, the intensity of the wind damage and its variation along the damage swath were not examined. Mou et al. (2001) described the detailed size and shape of four buildings damaged by a tornado spawned by Typhoon Kai-tak in Zhejiang Province. They, however, did not rate the damage in the Fujita (F) scale (Fig. 3; Fujita 1971a). Zheng (2009) roughly assigned F2–F3 intensities to a tornado based on the damage in a couple of locations, but did not provide a detailed distribution of the tornado intensity along the damage path. There was also a damage survey aimed at tornado verification (Tang and Liao 2007). In their half-page damage survey report, Tang and Liao stated that the damage swath was

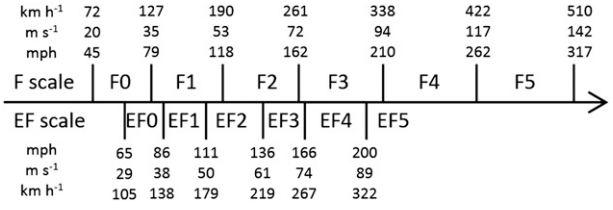

FIG. 3. The F vs EF scales for tornado ratings in terms of mi h^{-1} (mph), m s^{-1}, and km h^{-1}. The range for different scales starts from the left (e.g., 65 ≤ EF0 < 85 mph).

FIG. 4. Photographs of the fallen trees in Fig. 1c in south FT, in which the lowercase letters correspond to the different panels in this figure. (a) The authors and the watermelon farmer (in white T-shirt), who was injured by the tornado and was just dismissed from the hospital, standing in the center of the tornado path. (b) The convergent fallen trees north of an east–west-oriented road as highlighted by the large white arrows. (c) The fallen trees and corn stalks north of the road and west of the tornado center. (d) The fallen corn stalks south of the road and east of the tornado center. Both (a) and (b) were shot during the authors' first damage survey. The pictures in (c) and (d) were provided by Bato.cn. The red arrows in the bottom-right corner denote the direction that the photographer was facing.

narrow and some debris was scattered in different directions. They, however, did not provide any visual evidence for the claimed features. They assigned an F0 intensity to the tornado but did not mention either the intensity distribution or the damage indicators used for their rating. All in all, none of the previous tornado damage surveys published in China has provided a tornado track down to street resolution with the variation of tornado intensity along the track rated on the enhanced Fujita (EF) scale (Fig. 3; WSEC 2006) with the aid of visual evidence. Identifying the weather phenomenon responsible for the wind damage has not been examined with adequate visualized evidence either. The aim of the present reported study is to verify the tornado of 21 July 2012 in Beijing through the most detailed damage survey so far in China together with illustrations of radar-based supercell and tornado signatures in addition to analyses of their convective environment.

The remainder of this paper is structured as follows. The data are introduced in section 2 followed by a demonstration of tornado evidence disclosed in our damage surveys in section 3. Some radar signatures and environmental features associated with the damaging wind phenomena are described in section 4. Finally, our conclusions and a brief discussion are presented in section 5.

2. Data and methodology

The authors performed two on-site ground damage surveys. The first one was on 3 August 2012 (Fig. 4a). The authors investigated the damage in DXZ, ZLZ, and FT, interviewing 17 local people at 11 places along the damage path. Detailed information about the damage extent, sound, color, shape of the tornado, and falling directions of walls, trees, and telephone poles were obtained. The second damage survey was performed on 25 August 2012 for a more comprehensive examination and clarification of areas of confusion, during which further information was collected along the whole damage path through interviewing local government employees who had rushed to the damage area immediately after the tornado event to aid in the disaster recovery.

The photographs and videos of the aftermath provided by a variety of sources (M. Zhang, Bato.cn, Youku.com,

591hx.com, and Sina.com.cn) and shot on 21 or 22 July were additional sources of information aside from the authors' on-site damage surveys. Only part of the damage is shown in the figures. Through a careful identification and on-site verification, more information on the direction of debris falls and the damage extent was obtained.

The wind damage was rated at some places using the EF scale (Fig. 3; WSEC 2006). We tended to be conservative in ranking both the artificial-structure and tree damage indicators (DIs) considering the uncertainties associated with the differences in construction codes between China and the United States, as well as the complex impact of different factors associated with tree mortality such as size of trunk and crown in addition to soil properties (Frelich and Ostuno 2012; Blanchard 2013). All of the DIs were assigned the expected value (EXP) of wind speed estimation for the matched degree of damage (DOD).

The data used to analyze the storm environment included the Beijing rawinsonde and radar (both indicated by the red dot in Fig. 1b) observations, and the Final Analysis (FNL) of the Global Forecast System (GFS) of the National Centers for Environmental Prediction (NCEP). The Beijing radar is an S-band radar and is similar to the Weather Surveillance Radar-1988 Doppler (WSR-88D) operating in the United States in both its hardware and software (Zhu and Zhu 2004). The elevation of the radar antenna is 92.1 m above mean sea level (MSL) and 57 m above ground level (AGL). It operated in volume coverage pattern 21 (VCP21), which scans nine elevation angles including 0.5°, 1.4°, 2.4°, 3.3°, 4.3°, 6°, 9.9°, 14.6°, and 19.5° with a volumetric update time of 6 min during this event. The half-power beamwidth is 0.87° both in azimuth and elevation. The maximum unambiguous ranges for radar reflectivity Z_H and radial velocity V_R are 460 and 230 km, respectively. The Nyquist velocities are from -27 to 27 m s^{-1}. The azimuthal gate spacing at a range of 5 (15) km is ~90 (260) m. The gate width is 250 m. The Beijing rawinsonde station is collocated with the Beijing radar station, where a global telecommunication system electronic radiosonde is used in operation with an L-band radar to measure temperature, pressure, relative humidity, wind direction, and velocity from the ground to an altitude of 30 000 m AGL.

3. Evidence of the tornado based on damage surveys

Two distinguishing signatures of a tornado were found through our damage surveys. One is a narrow damage swath. The other is a convergent tree-fall pattern at multiple places along the swath.

a. Wind damage and the narrow damage swath

The damage swath was ~10 km long and 30–400 m wide (Fig. 1a, red shading). The first sign of the wind damage appeared northeast of HT at ~1340 LST. The tornado then moved to the northeast along a linear path through eastern DBG, northern XBG, FT, and ZLZ with an overall movement from ~195° at ~10 m s^{-1}, which was estimated with radar data. After entering ZLZ at ~1350 LST, the tornado started a sinusoidal track passing through DXZ and XDFZ. Similar nonlinear tracks have also been observed in U.S. tornadoes (e.g., Zrnić and Istok 1980; Wakimoto et al. 2003). The damage diminished in XDFZ at ~1400 LST.

In the early stage of its life cycle, the tornado leveled a ~5000-m^2 cornfield, approximately 100 m wide south of DBG. A locust tree ~50 cm in diameter in eastern DBG was debarked with only stubs of its largest branches remaining (Fig. 1a1, 1 in Fig. 5, the right-hand number in the notation of Fig. 1a1 refers to the label in the thumbnail images; the number in the notation of "number in Fig. 5" refers the label found in the map and column 1 in Fig. 5). This DI was assigned an EF3. The details of the EF ratings are given in Fig. 5, including the DI, DOD, damage description, and magnitude of the estimated wind speed and EF scales (WSEC 2006). Roofs of some buildings were totally removed (Fig. 1a2). Large branches of some trees at the same location were broken (B in Fig. 5; rated EF0). Farther to the north, aspen trees up to 25 cm in diameter at a distance of ~100 m were snapped (Fig. 1a3; 3 in Fig. 5; rated EF1). A wall ~150 m long (2 m high, free standing, and made of bricks with mortar) was flattened immediately south of Fig. 1a3.

On a watermelon farm south of FT (Figs. 1a4 and 4a), some farmers were thrown ~10 m to the north or northwest. As recalled by a farmer (Fig. 4a), the swirling air column went right toward them from the southwest at ~1345 LST and swept away their shed. An electrical transmission line pole (Fig. 1a4; 4 in Fig. 5; rated EF3) and trees ~10–20 cm in diameter over a distance of ~30 m farther east were snapped (Fig. 1a5; 5 in Fig. 5; rated EF1). Another tree ~30 cm in diameter farther west was uprooted (Fig. 4c, D in Fig. 5; rated EF1).

The tornado hit FT on the eastern edge of the village, where a mushroom farmer saw the funnel cloud enter the farm, destroy a corner of a building near the gate, and peel the roof of another building to the immediate north (E in Fig. 5; rated EF1). A mushroom greenhouse next to the impacted building was severely damaged. Another greenhouse ~20 m away from the damaged

Locations of the DIs	Location No.	DI	DOD	Damage description	Wind speed (mph)	EF scale
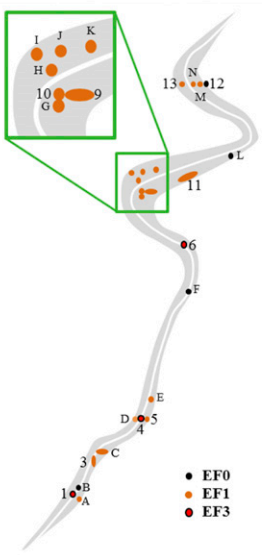	M,N,13	27. Trees hardwood (TH)	4	Trunks snapped	110	EF1
	12	18. Mid-rise building: 6 stories (MRB)	2	Loss of roof covering (<20%)	83	EF0
	L	27. Trees hardwood (TH)	2	Large branches broken	74	EF0
	9, 11	27. Trees hardwood (TH)	4	Trunks snapped	110	EF1
	G,10,H, I, J, K	27. Trees hardwood (TH)	3	Trees uprooted	91	EF1
	6	23. Warehouse building (WHB)	7	Total destruction of entire building	158	EF3
	F	9. Small professional building (SPB)	2	Loss of roof covering material (<20%)	78	EF0
	E	9. Small professional building (SPB)	5	Loss of significant roof covering material (>20%)	100	EF1
	D	27. Trees hardwood (TH)	3	Trees uprooted	91	EF1
	5	27. Trees hardwood (TH)	4	Trunks snapped	110	EF1
	4	24. Electrical transmission line (ETL)	5	Broken concrete poles	138	EF3
	C, 3	27. Trees hardwood (TH)	4	Trunks snapped	110	EF1
	B	27. Trees hardwood (TH)	2	Large branches broken	74	EF0
	1	27. Trees hardwood (TH)	5	Trees debarked with only stubs of largest branches remaining	143	EF3
	A	27. Trees hardwood (TH)	4	Trunks snapped	110	EF1

FIG. 5. Details of the EF ratings of the tornado damage at the 24 positions (first and second columns). The positions marked by numbers have corresponding photographs in Fig. 1a; the photographs for D, H, M, and N are shown in Figs. 4c, 6a, 7d, and 7b, respectively. The DIs, DOD, damage description, magnitude of the estimated wind speed, and EF scale are shown in different columns. All of the DIs were assigned the expected value (EXP) of wind speed estimation for the matched DOD.

building was not affected, which indicated the sharp gradient of the damage severity. Rating the damage to buildings is challenging because different countries or different areas in the same country may have different standards of building construction. The damaged buildings were compared to ''small professional buildings.'' This DI was used because they were single storied with a masonry-concrete structure and mansard roofs consisting of steel roof structures and tile roof coverings. All these features best match with the small professional buildings classification (WSEC 2006). The residences in this area are typically in this style.

Leaving FT, the tornado caused slightly weakened damage for a couple of minutes. In southern ZLZ, the tornado impacted a rectangular-shaped factory[1] that was bounded by brick walls on all sides. The tornado downed the wall of the factory for ~30 m along its west side, ~40 m on its south side, and ~50 m along its east side. Some people in the factory saw the swirling air column entering the factory and heard it roaring like a train while they were in a building in the northeast corner of the factory complex. A free-standing temporary cabin used to store tools immediately south of the building was blown away. Immediately to the east of the factory, trees up to 25 cm in diameter were uprooted and the roofs of some buildings, which were constructed in a similar way as the impacted buildings in the mushroom factory of FT, were partially damaged (F in Fig. 5; rated EF0). Heading toward northern ZLZ, the tornado caused increased damage at ~1350 LST. A worker in a factory (immediately south of Fig. 1a6) saw a swirling air column ~30 m wide pass right in front of his office. The factory to the immediate north was flattened, killing two people (Fig. 1a6). The roof of the factory was seen to be lifted off the building before crashing to the ground (6 in Fig. 5; rated EF3).

DXZ experienced the widest damage swath (~400 m in diameter) extending from the southwest to the northeast corner of the village. The residents recalled that the sky was filled with flying metal panels (indicated in Fig. 1a7), stones, bricks, tiles, sand, and branches of trees at the moment of the disaster. The roofs and walls of many buildings were blown away or totally destroyed (e.g., Fig. 1a8). Aspen trees with diameters of up to 30 cm within a distance of ~500 m on Zhangfeng (ZF) Road were uprooted (e.g., Fig. 6a; H in Fig. 5; rated EF1) or snapped. Trees within a distance of ~300 m on the west–east-oriented road were also snapped (Fig. 1a9; 9 in Fig. 5; rated EF1) or uprooted (Fig. 1a10; 10 in Fig. 5; rated EF1). Aspen trees up to 25 cm in diameter over a distance of ~100 m were also uprooted or snapped in

[1] By referring to ''factory,'' the authors mean the grounds of a factory instead of individual buildings.

FIG. 6. Photographs of the fallen trees in Figs. 1d,e in DXZ, in which the lowercase letters correspond to different panels in this figure. (a) A fallen tree (highlighted by the large white arrow) in the south-southeast direction, east of a north–south-oriented road. (b) The fallen trees in the east-southeast direction just across the street from the scene in (a), west of the north–south-oriented road. (c) A tree leaning in the south-southeast direction (highlighted by the large white arrow), west of the north–south road ~100 m farther north of the scene in (b). (d) Fallen trees in the north-northeast direction, south of a west–east-oriented road in the southwest corner of the village. (e) A fallen tree in the east-northeast direction along a road immediately neighboring the west–east-oriented road in (d), east of the south–north-oriented road. (f) The fallen trees in the north-northwest direction on the eastern edge of the village. The red arrows in the bottom-right corner of each panel denote the direction that the photographer was facing. The pictures in (a)–(c) are snapshots from a video provided by Youku.com. The pictures in (d) and (e) were provided by M. Zhang. The picture in (f) was shot by the first author.

eastern DXZ (Fig. 1a11; 11 in Fig. 5; rated EF1). Many telephone poles in the village fell or leaned after the storm. The damage on the right side of the centerline of the damage path was more severe than that on the left side, which faced the direction in which the tornado was moving, similar to the observations of some U.S. tornadoes (e.g., Davies-Jones et al. 1978; Alexander and Wurman 2005).

Crossing the Jingha (JH) Highway, the damage path was manifested as a pronounced sinusoidal wave pattern before the tornado finally diminished. The tornado left a damage path ~100 m wide with fallen trees or destroyed factory rooftops during the first turn west of Shaojiuxiang (SJX). During the storm's second turn, the tiles on the roof of some steel-reinforced concrete buildings were peeled off in XDFZ (Fig. 1a12; 12 in

FIG. 7. Photographs of the fallen trees in Fig. 1f north of a west–east-oriented road on the southern edge of XDFZ, in which the lowercase letters correspond to different panels in this figure. The (a) western and (b) eastern ends of the downed wall. (c) As in (a), but ~20 m to the west with an eastward fallen tree. Shown in (b) is a westward fallen tree near the eastern edge of the downed wall. (d) As in (b), but ~30 m to the east, also showing a westward fallen tree. The red arrows in the bottom-right corner denote the direction that the photographer was facing. The pictures were snapshots from a video provided by Youku.com.

Fig. 5; rated EF0). Many windows on the eastern and southern sides of the buildings were broken. Frames of some windows were even pushed totally inside (Fig. 1a12). The metal frames of some bicycle sheds with supporting pillars set ~25 cm deep into concrete were pulled out. Some motorcycles were blown away. A minivan was seen being blown to the other side of the street. A 50-m-long wall was blown down in the southwest corner of the town with trees up to 15 cm in diameter snapped (e.g., Fig. 1a13; 13 in Fig. 5; rated EF1). The last observed damage was to a wall that was downed ~20 m northeast of XDFZ.

To summarize, the above damage analyses demonstrate that the tornado had a damage swath ~30–400 m wide and ~10 km long. The damage at three places along the damage path was rated EF3. The severity of the wind damage rapidly increased to EF3 only a couple of minutes after its initiation. The damage severity weakened slightly near the middle point of the storm's path followed by a reintensification, as shown in the most extensive destruction in DXZ. The damage remained EF1 for a few minutes before finally diminishing at ~1400 LST in northern XDFZ.

b. *Surface convergent winds*

In addition to a narrow swath, convergent tree-fall patterns were found at different stages of the tornado, indicating convergent wind near the ground, which is another and more crucial distinguishing signature of a tornado.

At the watermelon farm south of FT (Figs. 1c and 4), the convergence was demonstrated by the leaning trees in the woods north of the road just across from where the farmers were working (Fig. 4b; refer to b in Fig. 1c). Along the road, corn stalks and trees ~30 m west of the damage center fell to the south or southeast (Fig. 4c; refer to c in Fig. 1c). In a shed ~30 m east of the damage center, the metal roof was turned up along its southern side, indicating a northward wind. A cornfield of ~400 m^2 near the shed was leveled with all of the corn stalks falling toward the north or northwest (Fig. 4d; d in Fig. 1c). This result indicated the convergent surface flow near the tornado center with more cyclonic rotation farther outward.

Convergent surface winds were also demonstrated by tree fall in DXZ. Most of the trees and debris north of the southwest–northeast-oriented tornado track were blown over to the east or southeast (Figs. 6a–c; refer to a–c in Fig. 1d), whereas those south of the tornado track were blown over to the north or northeast (Figs. 6d–f; d and e in Fig. 1d and f in Fig. 1e).

Convergent surface winds were again indicated in XDFZ. Along the road where a ~50-m-long wall was downed (the western edge was shown in Fig. 7a; the eastern edge in Fig. 7b), the trees west of the collapsed wall fell to the east (Fig. 7c; c in Fig. 1f), whereas the

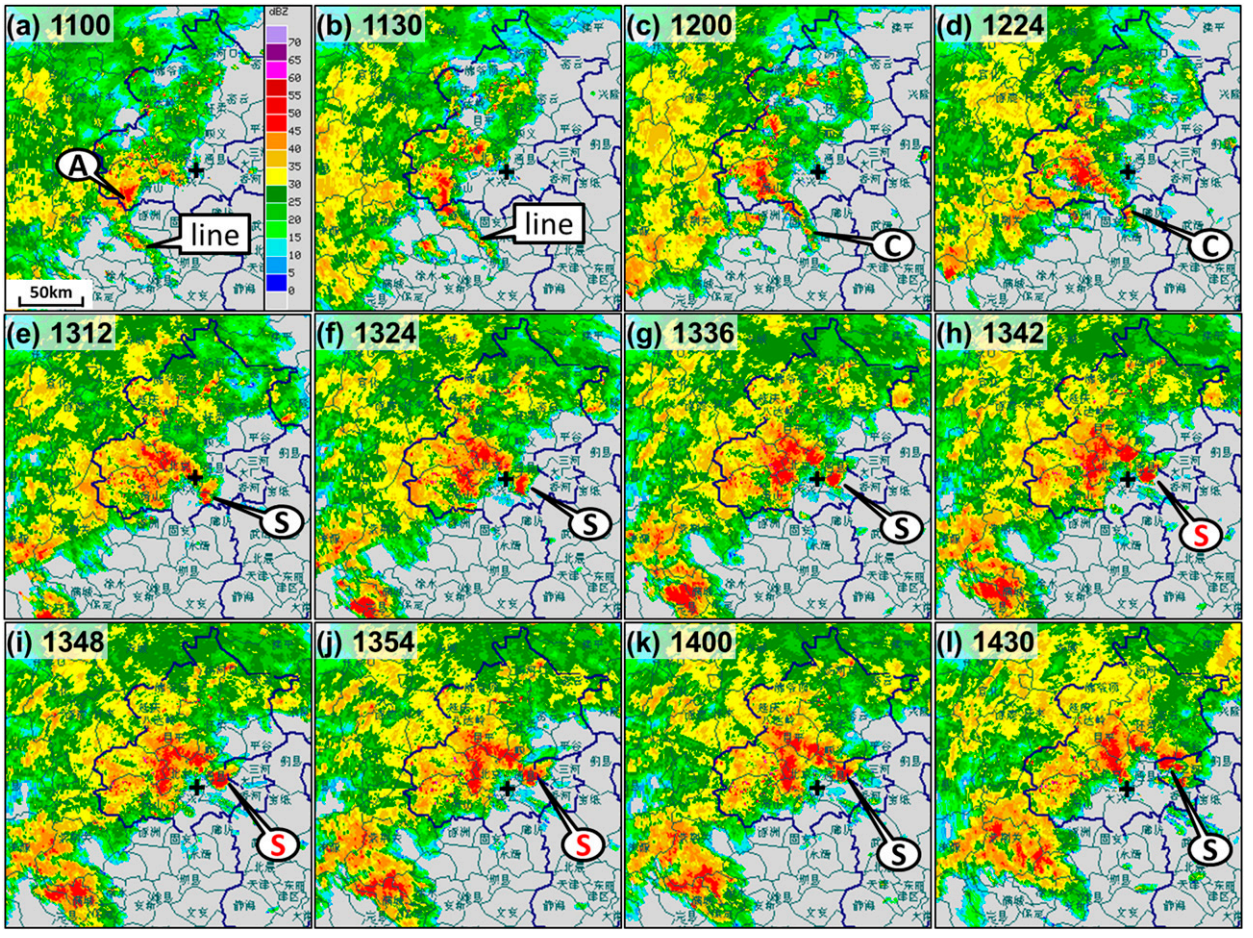

FIG. 8. The evolution of Z_H at 0.5° PPI showing the squall line (denoted by "line"), the isolated cell (denoted by C), and the tornadic supercell (denoted by S, where red represents the time when the tornado damage was occurring). The radar station at Beijing is marked by the black cross. The map scale is given in the bottom-left corner of (a). Letter A denotes a convective system to the northwest of the convective line.

trees east of the collapsed wall fell to the west (Figs. 7b and d; b and d in Fig. 1f).

With the two apparent signatures that consisted of the narrow damage swath and surface convergent flow at multiple spots along the tornado track in place, it is clear that the wind damage in southeastern Beijing was caused by a tornado. This EF3 tornado will be referred to as "the Beijing tornado" in the remaining sections.

4. Observational analysis of the Beijing tornadic supercell and its environment

a. Radar signatures of the supercell and the tornado

1) THE SUPERCELL AND THE MESOCYCLONE

The Beijing tornado was embedded within a supercell that developed at the southern end of a northwest–southeast-oriented squall line (Fig. 8). The squall line became apparent at 1100 LST when it was moving northeastward to Beijing. It intensified at 1130 LST after merging with a convective system to its northwest (A in Fig. 8a). A cell at the southern tip of the squall line intensified at 1200 LST and separated from the squall line at 1224 LST. The cell met the threshold of a supercell as defined by Smith et al. (2012) at 1312 LST and matured at 1348 LST. The supercell then dissipated and lost its identity at 1600 LST.

Detailed structures of the supercell were analyzed using the level-II data of the Beijing S-band Doppler radar, which was located ~20 km west of the tornado at ~1340 LST. The analysis was performed with the Gibson Ridge radar viewer GR2Analyst (http://www.grlevelx.com/), which has been used for other radar analyses in the literature (e.g., Smith et al. 2012). The supercell was much better organized in terms of the morphology of the 40-dBZ contour of Z_H at 2.4° plan

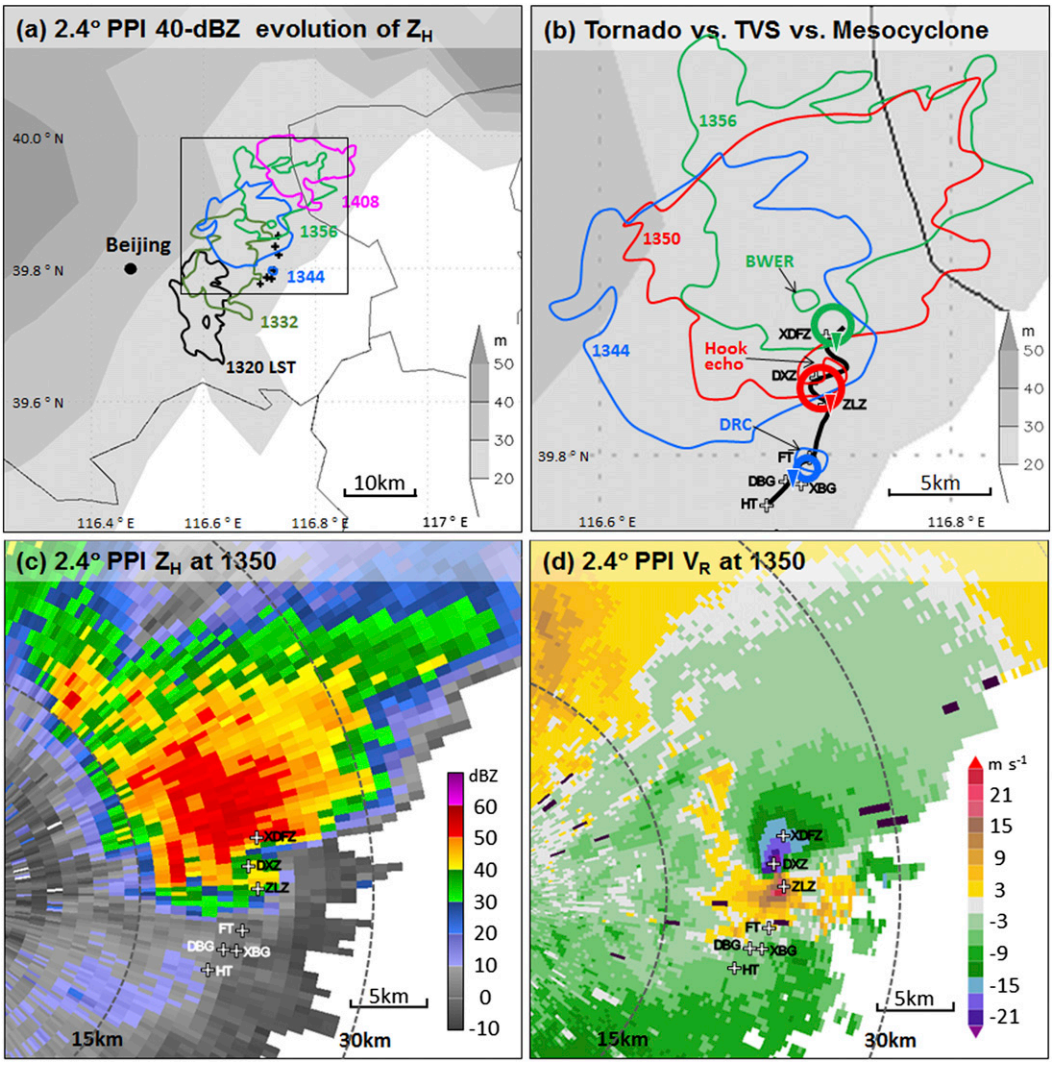

FIG. 9. (a) The evolution of Z_H of the supercell in terms of the 40-dBZ contour of Z_H at 2.4° PPI between 1320 and 1408 LST every 12 min. (b) The enlarged area denoted by the rectangle in (a) with 1350 LST added. Also plotted in (b) are the hook echo at 1350 LST, the bounded weak echo region (BWER) at 1356 LST, the DRC at 1344 LST, the tornado track (black heavy curve), the mesocyclone on 2.4° PPI (solid circles denoting the diameter of the mesocyclone), and the 0.5° PPI TVS locations (denoted by the bottom tip of the triangles) in the duration of the damage with different times shown in different colors. The topography is shaded progressively darker every 10 m. The large black dot in (a) denotes the rawinsonde and radar station at Beijing. Snapshots of 2.4° PPI (c) Z_H (dBZ) and (d) V_R (m s^{-1}) at 1350 LST. The crosses denote the affected villages.

position indicator (PPI; Figs. 9a,b) with a well-defined hook echo and a weak echo region (WER) during the period when tornado damage was observed (~1340–1400 LST) compared to the period before and after. The Z_H and V_R at 2.4° PPI at 1350 LST are shown in Figs. 9c,d, respectively. The hook echo overlapped an apparent mesocyclone, as indicated by a couplet of V_R (Fig. 9d). The mesocyclone at 2.4° PPI at 1350 LST had a diameter of ~2 km. The diameter of the mesocyclone was defined as the distance between its maximum inbound V_i and outbound V_o radial velocities (Stumpf et al. 1998). A mesocyclone has usually been defined as a concentrated area of vertical vorticity larger than a certain threshold [e.g., 0.01 s^{-1} in Glickman (2000) and WDTB (2013a); 0.005 s^{-1} in Donaldson (1970)] in conjunction with a supercell updraft. The parent mesocyclone associated with the Beijing tornado exceeded these vorticity thresholds.

The intensity of the mesocyclone was estimated using the mesocyclone strength nomogram (Fig. 10; Andra 1997; Stumpf et al. 1998; Lee and White 1998). Notably, the nomogram was designed by Andra (1997) for

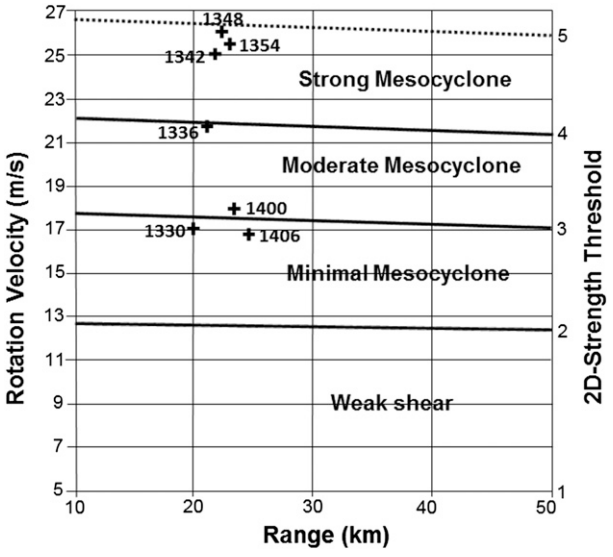

FIG. 10. The peak rotational velocity of all of the elevation angles at each time during 1330–1406 LST for the Beijing case (marked by crosses) using the mesocyclone strength nomogram adapted from Fig. 1 of Lee and White (1998) and the same nomogram but in unit of m s^{-1} (available online at http://www.meted.ucar.edu/radar/severe_signatures/print_midlevel_mesocyclone.htm). Regions of the weak shear, and minimal, moderate, and strong mesocyclone are divided by thick lines. Each region is defined by a 2D strength threshold labeled 1–5 to the right. [The value of 5 was not included in Fig. 1 of Lee and White (1998). It is added here following the rate of change from 2 to 4 to accommodate the values >4.]

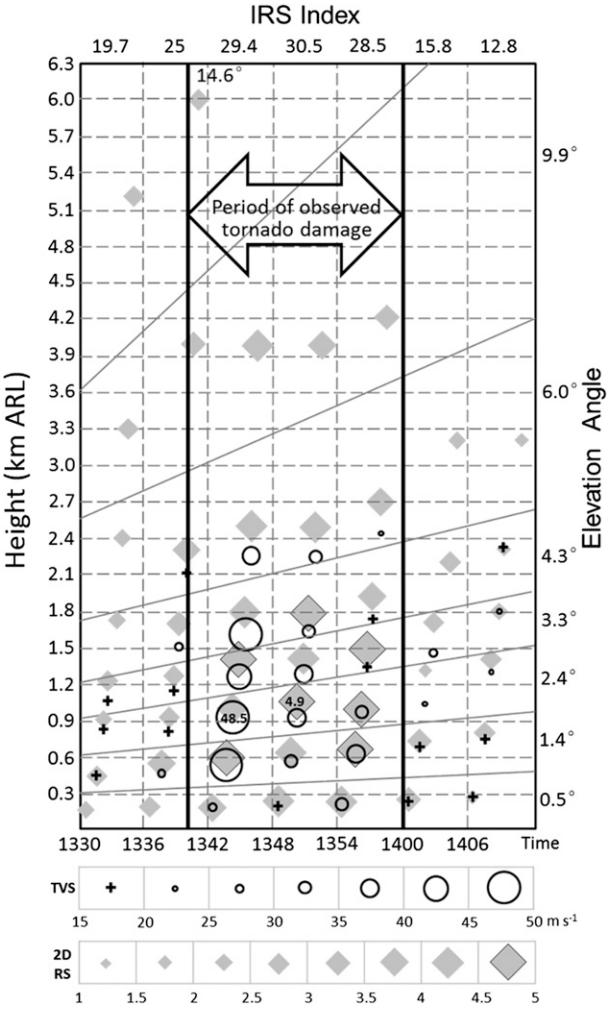

FIG. 11. Vertical distribution of the intensity of the vortex signature (circles) and 2D-RS (shaded diamonds) during 1330–1406 LST every 6 min with the respective maximum values denoted by the numbers. The crosses denote the vortex signature with an intensity of 15–20 m s^{-1}. The intensity scales are given along the bottom. The diamonds with black edges denote 4.5 ≤ 2D-RS < 5. The period of observed tornado damage is denoted by the two thick lines connected by a large two-way arrow. Also displayed along the top are the integrated RS (IRS) indices indicating the overall strength of the mesocyclone.

a mesocyclone with a diameter of 6.5 km, which was ~3 times as large as the Beijing case; thus, the slope of the lines dividing the regions should be slightly steeper for this case (Lee and White 1998). Comparing the peak rotational velocity at all elevation angles at each time from 1330 to 1406 LST to the thresholds of rotational velocity of Andra (1997) (Fig. 10, solid diagonal lines), it was found that the Beijing mesocyclone (Fig. 10, crosses) evolved from a minimal mesocyclone at 1330 LST into a strong mesocyclone during 1342–1354 LST and then weakened back to a minimal one at 1406 LST. The maximum rotational velocity of the mesocyclone was 26 m s^{-1}. This result was consistent with the statistics of Smith et al. (2012). They used the same mesocyclone nomogram to show that about 90% of EF3–EF5 tornadoes were associated with strong mesocyclones. The intensity of the mesocyclone was also measured in terms of its two-dimensional rotational strength (2D-RS) using the right ordinate labeled as the 2D-strength threshold in Fig. 10 (Lee and White 1998). The 2D-RS of the mesocyclone during the damage period was much higher than 4 in the Beijing case.

The time–height variation of the 2D-RS of the Beijing mesocyclone (Fig. 11, shaded diamonds) showed that the intensification of the mesocyclone during the period of severe damage was observed at all elevation angles with the maximum values appearing between 0.5 and 2 km above radar level (ARL). The coincidence between the strong mesocyclone and the tornado was clearly shown in the larger (relative to other times) near-surface 2D-RS and the integrated RS (IRS) indices [the summation of the 2D-RS at all elevation angles from circulation base to top as defined by Lee and White (1998); Fig. 11, the top ordinate]. The height of the mesocyclone was 6 km ARL at its onset and decreased to ~3 km ARL before dissipating.

The tornado track was closely related to the features of the mesocyclone. First, the period of the tornado damage was overlapped with the period during which the mesocyclone was strong. The tornado damage had two peaks in severity at ~1344 and ~1350 LST, respectively, whereas the intensity of the mesocyclone remained quite steady in terms of the IRS. The increased damage at ~1350 LST might be associated with the expansion of the mesocyclone. The expansion was clearly shown in the increase of the mesocyclone diameter at 2.4° PPI from ~1 km at 1344 LST to ~2 km at 1350 LST (Fig. 9b, solid circles), which was quite consistent with the variation of the corresponding 2D-RS at 2.4° PPI (Fig. 11). Second, the sinusoidal track of the tornado starting at ~1350 LST may have resulted from the expansion of the mesocyclone at the same time (Fig. 9b). The tornado had a linear track before it reached ZLZ when the mesocyclone was small. When the diameter of the mesocyclone increased to ~2 km shortly afterward, the tornado started to assume a sinusoidal track with a similar amplitude. This result suggests that the sinusoidal track of the tornado was probably due to the rotation of the tornado around the mesocyclone, as proposed by Zrnić and Istok (1980) and Wakimoto et al. (2003). Since deviations by a tornado from its originally linear track have been frequently observed in the later stage of a tornado's life span (e.g., Fujita 1971b, 1974; Agee et al. 1976; Bluestein 1983; Wakimoto et al. 2003), it would be interesting to examine how often the expansion of the parent mesocyclone would appear in the later stage of a tornado's lifetime when the tornado displayed a nonlinear track. This is, however, beyond the scope of the current study.

2) TVS

A tornadic vortex signature (TVS) is a Doppler velocity signature of a tornado or an incipient tornado-like circulation aloft (Burgess et al. 1975a,b; Brown et al. 1978; Glickman 2000). TVSs were detected in the mesocyclone of this present reported case. There have been different criteria for TVS detection in the literature (e.g., Brown et al. 1978; Trapp et al. 1999; French et al. 2013; WDTB 2013b). Brown et al. (1978) determined a TVS to be a four-dimensional feature using the following criteria: 1) azimuthal shear of at least 20 m s^{-1} over an azimuthal distance of approximately one beamwidth; 2) a signature with extreme Doppler velocity values of opposite sign, after TVS translation has been removed; 3) an anomalous shear region not more than about 1 km in range extent; 4) a shear region of at least several kilometers in the vertical extent; and 5) a persistent anomalous shear region at the same general heights for about 10 min or more. WDTB (2013b) used more relaxed TVS criteria that consisted of a 1.5-km depth and 5-min duration. French et al. (2013) defined a TVS as a two-dimensional feature: a cyclonic shear signature that matched up with the time and location of a known tornado if the gate-to-gate azimuthal radial velocity difference (ΔV) was at least 20 m s^{-1} over a distance no greater than 2 km. In this work, two-dimensional TVSs were detected at different elevation angles using the first three conditions of Brown et al. (1978). The evolution of thus-determined TVSs at 1.4° PPI is plotted in Figs. 12a–d. These TVSs were also manifested as strong localized rotations [Figs. 12f–i in terms of normalized rotation (NR[2])]. The time–height profile of the magnitude of the TVSs and the vortex signatures that did not meet the 20 m s^{-1} criteria but that were larger than 15 m s^{-1} are plotted as circles and crosses in Fig. 11, respectively.

The time period during which severe damage was observed was perfectly coincident with that during which the TVSs and their parent mesocyclone had their largest magnitude (Fig. 11). The first TVS was detected at ~1337 LST at 0.5 km ARL near HT. About 1 min later, a TVS was detected at 1.5 km ARL. In the next 6 min, the TVSs intensified rapidly and were detected at all elevation angles below 9.9°. Associated with the intensification and downward development of the TVSs, the first damage was observed near HT at ~1340 LST. A TVS was detected at the lowest scan near DBG at 1342 LST. It was precisely overlapped with the beginning of severe damage exemplified by a debarked tree (rated EF3). The strongest TVS was detected at the same time ~1 km ARL at 2.4° PPI with a magnitude of 48.5 m s^{-1} (Figs. 12e,j).

The strength of the vortex weakened in the lowest nine elevation angles by 1348 LST and fell below the TVS ΔV criteria at the 0.5°-elevation angle, which thus made the TVS undetectable near the ground. This decreased azimuthal shear near the ground was coincident with the short-term weakening of the damage between FT and ZLZ. At 1354 LST, the vortex reintensified into a TVS in the lowest two elevation angles with a larger magnitude at the lowest elevation angle than at 1342 LST. This stronger TVS near the ground was closely associated

[2] NR is a product of GR2Analyst, which denotes the intensity of vertical rotation. NR is calculated in a way similar to the local, linear least squares derivatives (LLSD; Smith and Elmore 2004) method. In details, at each dealiased basic velocity bin, a 2-D filter that simultaneously fits a second order surface to, and takes the azimuthal gradient of, the 5 × 5 (3 × 3 when not enough) surrounding bins is applied. This gives the true rotation. It is then normalized to overcome the dependence of the retrieved rotation value on the observation range and hence obtain the NR. The range of NR spans between −5 and +5. Anything above 1.0 is significant and values above 2.5 are extreme.

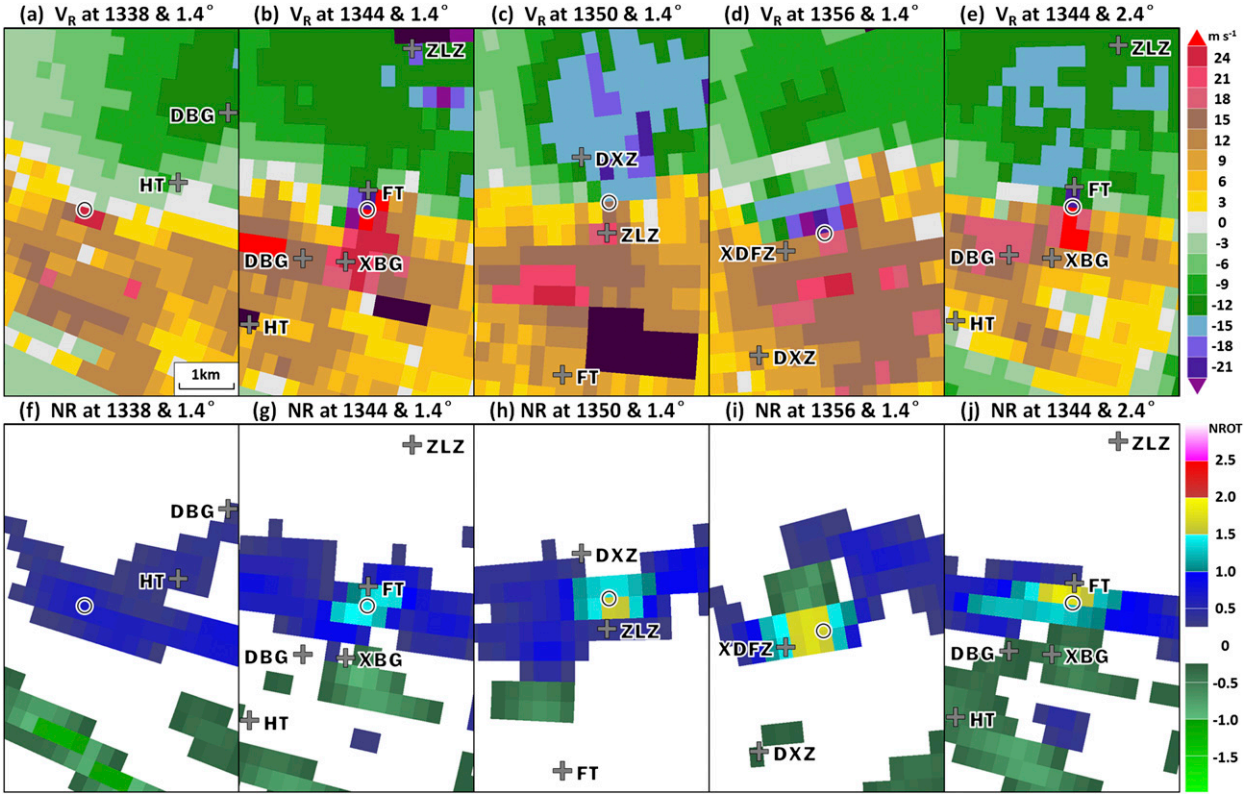

FIG. 12. The evolution of the TVS (black circles) on 1.4° PPI from 1338 to 1356 LST at an interval of 6 min overlaid on the ground-relative (a)–(d) V_R and (f)–(i) NR. Note that (e) and (j) are the same as other panels but for 1344 LST at 2.4° PPI, where the strongest TVS was detected during the whole process.

with the increased damage of the tornado with a wider damage swath in DXZ.

Starting at ~1400 LST, the TVSs substantially weakened and became undetectable at the lowest two levels, which were closely associated with the end of the observed damage in northern XDFZ. The vortex signatures were sustained for another 12 min at an altitude of 1–1.5 km ARL and dissipated thereafter.

3) DRC

Descending reflectivity cores (DRCs) were also detected in the Beijing tornado case. A DRC is a precipitation protuberance that is a pendant from the echo overhang of the rear side of the weak echo region of a supercell (Rasmussen et al. 2006). Starting from 1324 LST, which was ~15 min before the first observed damage from the tornado, an echo appendage became apparent above 2.4°-elevation angle (Figs. 13a,b) with an embedded maximum value meeting the criteria of Rasmussen et al. (2006). The three-dimensional isosurface of Z_H, which was generated by GR2analyst using bilinear interpolation, showed a bloblike pendant along the 50-dBZ isosurface from the echo overhang of WER. The pendant descended to near the ground at 1330 LST, indicating the occurrence of a DRC (Fig. 13, DRC1). The embedded local maxima of Z_H exceeded the minimum Z_H along the path of greatest Z_H from the DRC Z_H maximum to the supercell core by at least 4 dB (referred to as 4-dB criteria hereafter) at several elevation angles at this time (Fig. 14a, black circles). We noticed that the Z_H maxima in the appendage at 2.4° met the 4-dB criteria but did not ensure vertical continuity. The detection of a DRC requires considering the vertical continuity to guarantee a pendant feature. The Z_H maximum at one elevation angle needs to be continuous with those immediately above and below it. Those Z_H maxima that did not meet the 4-dB criteria but ensured a reasonable vertical continuity are marked by white circles in Fig. 14. Similar to previous studies (e.g., Rasmussen et al. 2006), DRC1 was associated with apparent jetlets accompanied by markedly counterrotating vortices (Fig. 14b) with the cyclonic vortex closely associated with the mesocyclone (Fig. 13c) at all nine elevation angles at 1330 LST. The counterrotating vortices were also clearly shown as the vorticity couplet in the 3D NR (Fig. 13d).

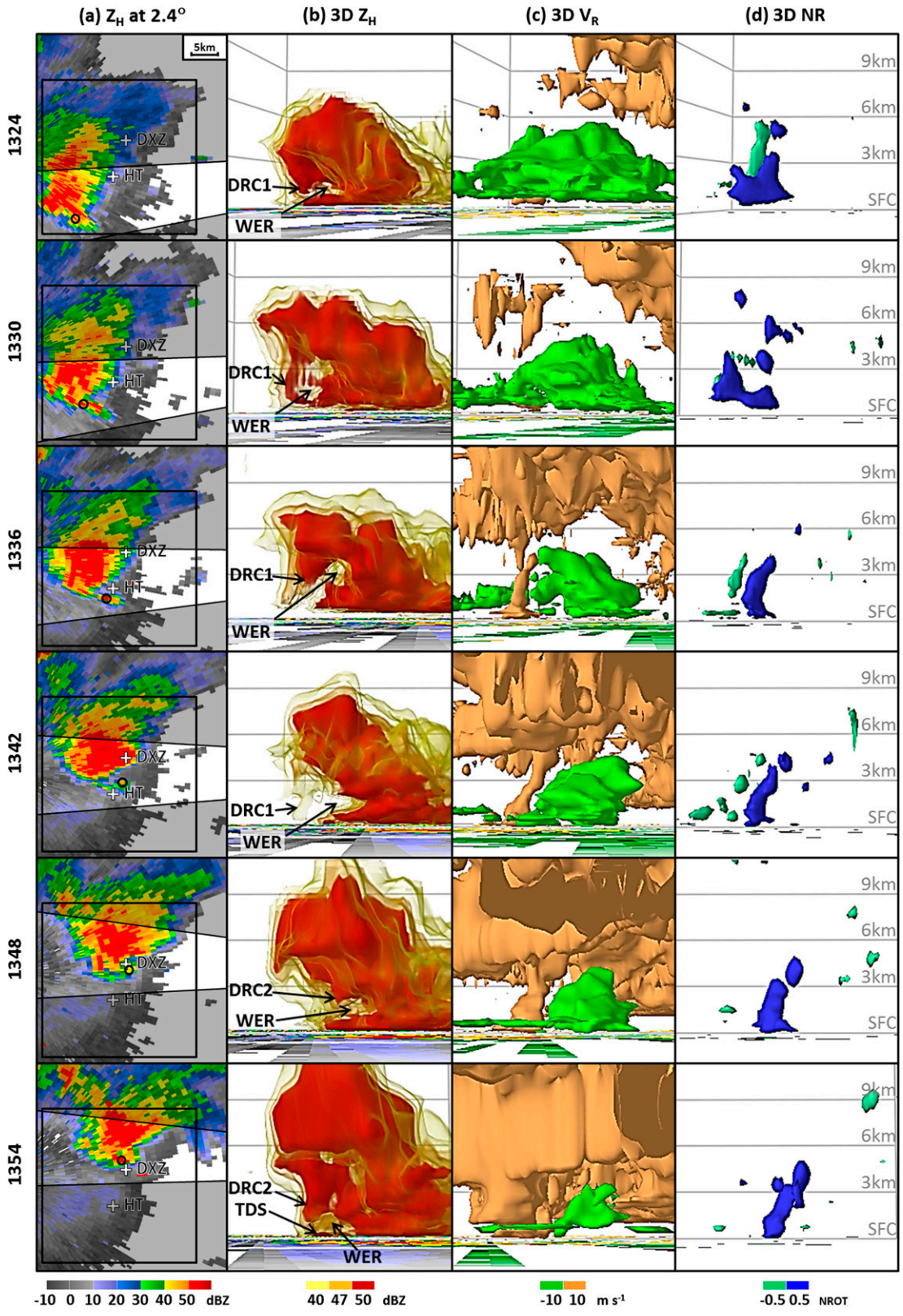

FIG. 13. The evolution of the DRCs from 1324 to 1354 LST in terms of (a) Z_H at 2.4° PPI (denoted by the black circles) and (b) the three-dimensional views of Z_H. Also shown are the corresponding three-dimensional (c) V_R and (d) NR results. All the three-dimensional figures were produced with the same angle of view and horizontal extent as denoted by the black squares in (a). Only the parts near the DRCs over the horizontal extent denoted by the highlighted areas in (a) are shown for detail in (b)–(d).

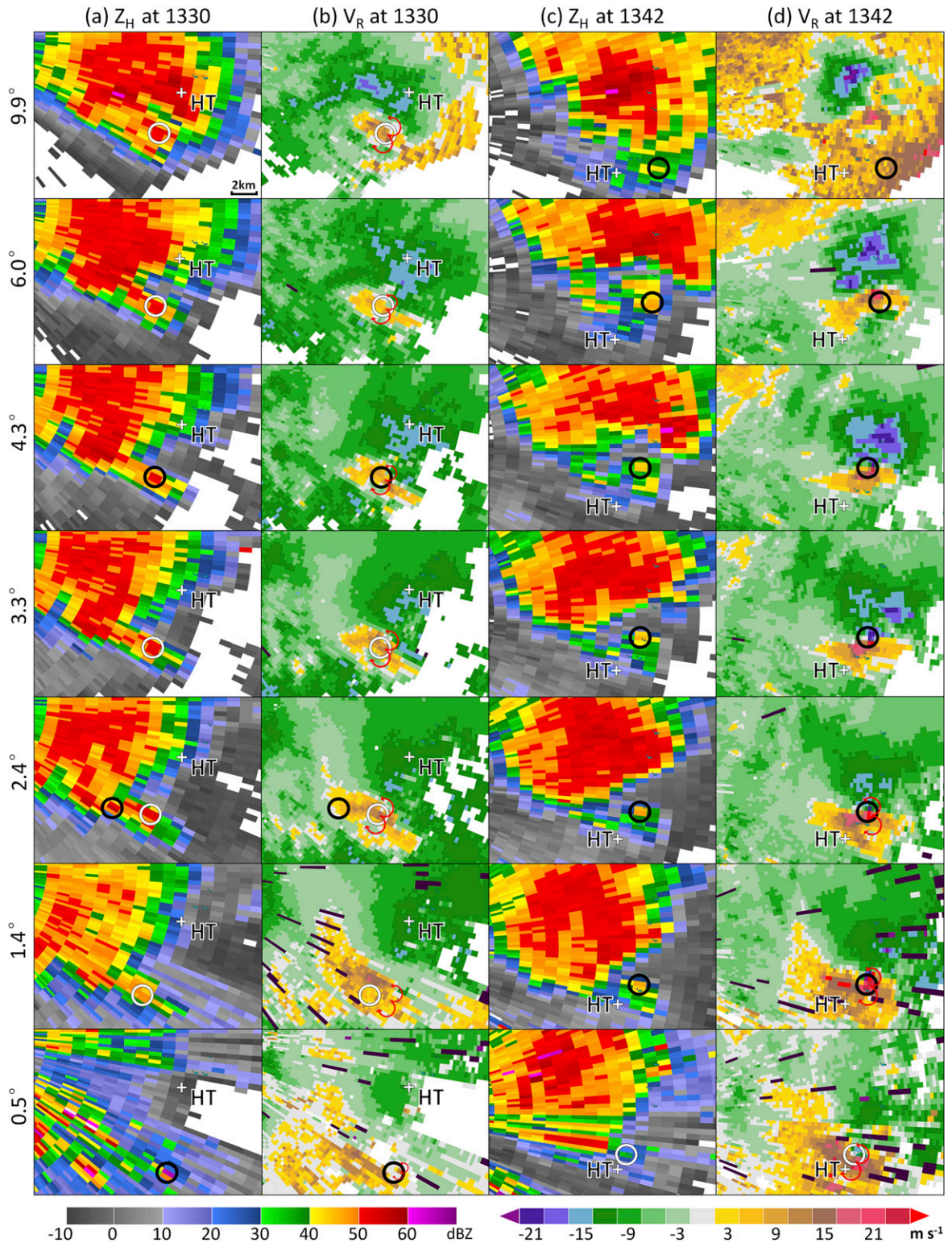

FIG. 14. Examples of DRC at (a) 1330 and (c) 1342 LST, as detected in Z_H at 0.5°, 1.4°, 2.4°, 3.3°, 4.3°, 6.0°, and 9.9° PPI. The Z_H maxima that satisfied the 4-dB criteria are denoted by black circles. The others are denoted by white circles. The corresponding V_R, together with the counterrotating vortices (red semicircles) caused by the jetlet associated with the DRC, is also shown in (b) and (d). The circles in (a) and (c) are also plotted in (b) and (d) for reference.

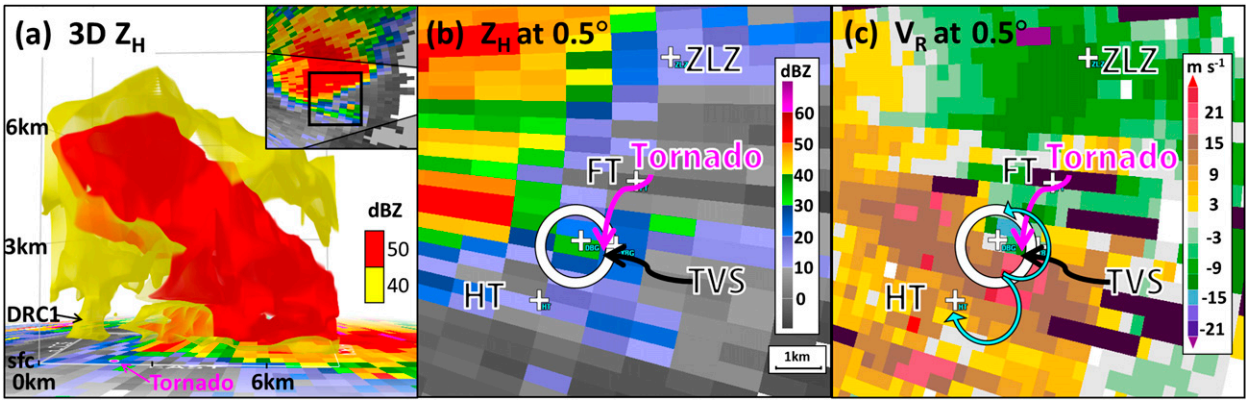

FIG. 15. Zoomed-in picture of DRC at 1342 LST in terms of the (a) isosurface, (b) 0.5° PPI of Z_H, and (c) 0.5° PPI of V_R. The DRC is marked with solid white circles in (b) and (c). The sense of the Doppler shear is illustrated with the curved cyan arrows. Also marked are the locations of the TVSs at the lowest scan and the tornado.

An interesting result was that the tornado was spawned during the upward shrinking process of DRC1, and DRC1 continued to shrink upward after tornadogenesis (Fig. 13b). At 1336 LST, which was a couple of minutes before the first sign of tornado damage, the 50-dBZ isosurface shrunk upward while the 40- and 47-dBZ isosurfaces still remained near the ground. At 1342 LST, when the TVS was the strongest and the severe tornado damage started to appear, only the isosurface at 40 dBZ remained near the ground (Fig. 13b, which is enlarged in Fig. 15a). The reason for the possible connection between the tornadogenesis and the upward shrinking of the DRC awaits further studies. Although DRC1 weakened at this time in terms of the maximum reflectivity, the 4-dB criteria, however, was met at all elevation angles except for 0.5° PPI (Figs. 14c and 15a). The Z_H maximum at 0.5° PPI right below the maxima of 1.4° PPI was still localized to a certain extent (Fig. 15b), thus, it maintained a reasonable vertical continuity of the DRC at all elevation tilts (Figs. 14c and 15a) although it failed to meet the 4-dB criteria at 0.5° PPI. More importantly, the cyclonic vortex associated with DRC1 and the TVS at 0.5° PPI and the observed tornado damage perfectly overlapped each other at this time (Fig. 15c). The anticyclonic vortex weakened with time, which was clearly shown in both the PPI V_R (Fig. 14d) and 3D NR (Fig. 13d) results.

DRC1 lost contact with the ground and its identity in terms of the 40-dBZ isosurface at 1348 LST, while a new, stronger, and wider DRC (DRC2 in Fig. 13b) developed from the middle of the echo overhang above the WER. This feature appeared right before the increased damage. The negative vorticity column became almost undetectable during the evolution of the DRC2 from 1348 to 1354 LST, likely due to the expanded mesocyclone (Figs. 13c,d). The above analyses demonstrate that the genesis and intensification of the Beijing tornado were closely associated with the appearance of the preceding DRCs. Considering the mixed results on the relationship between DRC and tornadogenesis in the literature (e.g., Rasmussen et al. 2006; Kennedy et al. 2007; Byko et al. 2009; Markowski et al. 2012a,b), the extent to which the formation of the Beijing tornado was related to the preceding DRC awaits further examination.

4) TDS

A tornadic debris signature (TDS) was detected at 1354 LST near XDFZ (Fig. 13b; the enlarged figure is shown in Fig. 16a). A TDS is defined as a tornadic signature ~1 km wide and 1–3 km high mainly using polarimetric radar variables (Ryzhkov et al. 2005). It is also referred to as an "echo dot" in Bunkers and Baxter (2011). The TDS was identified as a bloblike reflectivity isosurface of 50 dBZ and ~1.6 km wide near the ground (Figs. 16a,b) in this current case, and it may have been caused by the debris lifted by the tornado. The maximum reflectivity of 54.5 dBZ near the ground (Fig. 16b) fell well within the range of Z_H used to define a TDS as proposed by Ryzhkov et al. (2005). Though the TDS designation was not completely warranted due to the lack of polarimetric radar observations in this case, it was highly probable considering the following evidence (Bunkers and Baxter 2011): 1) the localized maximum in Z_H occurred near the tip of the hook echo (Fig. 16b); 2) the bloblike echo appeared at XDFZ when the tornado was occurring, thus being paired with corroborating ground truth information (Fig. 16b); 3) the Z_H of the bloblike echo was the greatest near the ground and gradually decreased with height (Fig. 16c); and 4) the bloblike echo was preceded by and associated with a strong TVS (Figs. 16d and 11).

The above radar analyses demonstrate further evidence for the occurrence of the tornado in the seven

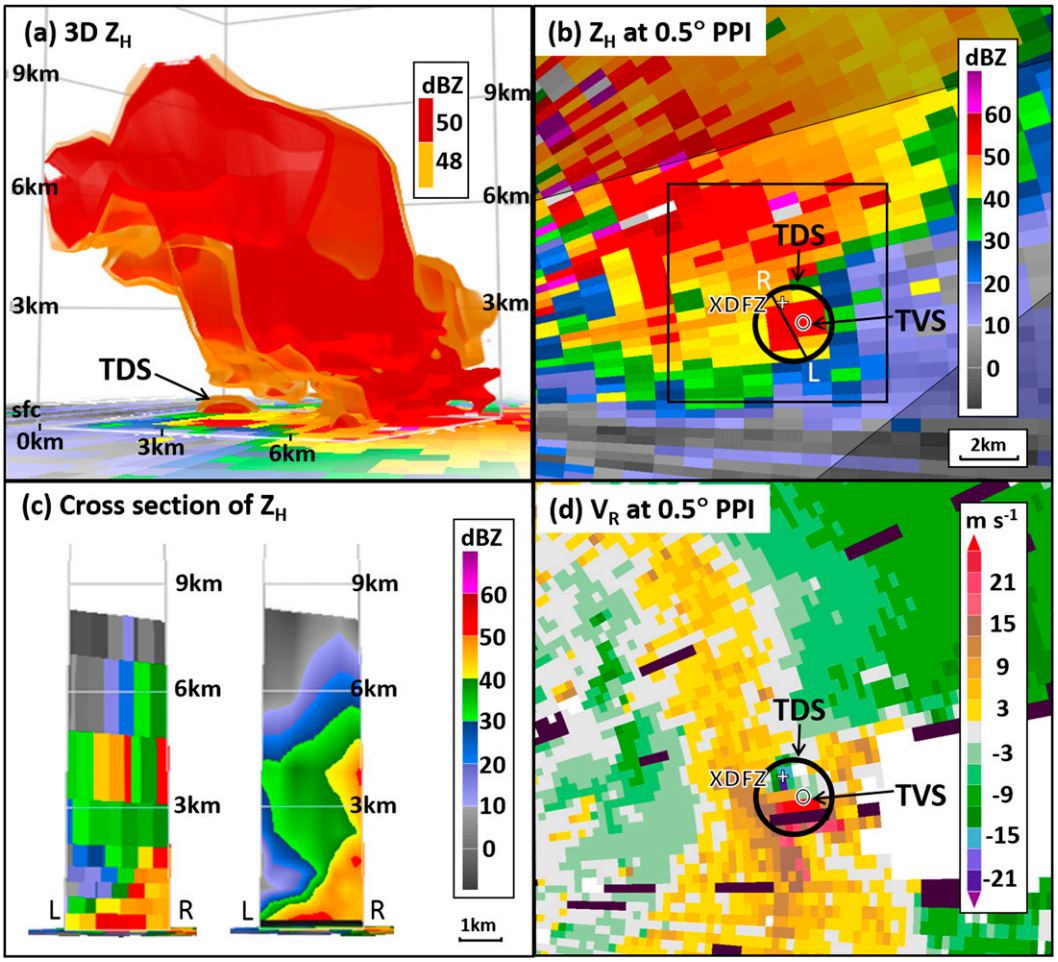

FIG. 16. The TDS at 1354 LST near XDFZ in terms of (a) 3D Z_H in the horizontal extent [denoted by the black square in (b)], (b) Z_H at 0.5° PPI, (c) the vertical cross section of Z_H [along the black line in (b) in terms of the original (left) Z_H and (right) the smoothed case], and (d) V_R at 0.5° PPI. The TDS and TVS are marked by the large and small black circles, respectively, in (b) and (d).

villages around southeastern Beijing during ~1340–1400 LST on 21 July 2012, including the mesocyclone, TVS, DRC, TDS, and the collocation of these radar signatures with wind damage, especially the coincidence of the TVS with the damage in terms of its location, timing, and intensity variation.

b. *The environment of the supercell*

The supercell formed in a favorable environment. A westerly trough embedded within a cold vortex (a quasi-stationary low pressure system with an upper-level cold core) remained west of Beijing at 500 hPa (Figs. 17a,b), implying ascent that favors convection development. The subtropical high remained southeast of Beijing. More to the south, Typhoon Vincent was located west of Luzon Island moving toward the southeast coastal area of China, and a quasi-stationary low pressure system was sustained in Bay of Bengal. Below the 500-hPa trough was a mesoscale cyclonic vortex at 700 and 850 hPa (Figs. 17c–f). The vortex moved much closer to Beijing from 0800 to 1400 LST. Associated with the approach of the mesoscale vortex, the low-level jet substantially intensified, especially at 700 hPa, transporting abundant moist and warm air northward to Beijing. As shown in the distribution of the column-integrated precipitable water (Figs. 17a,b, shaded) and the water vapor mixing ratio at 700 and 850 hPa (Figs. 17c–f, shaded), the moisture immediately south of Beijing clearly increased during the 6-h period. The low-level warming and moistening created an increasingly unstable environment over Beijing.

The increases of the environmental instability and low-level vertical shear from 0800 to 1400 LST were further shown by the Beijing rawinsonde, which was

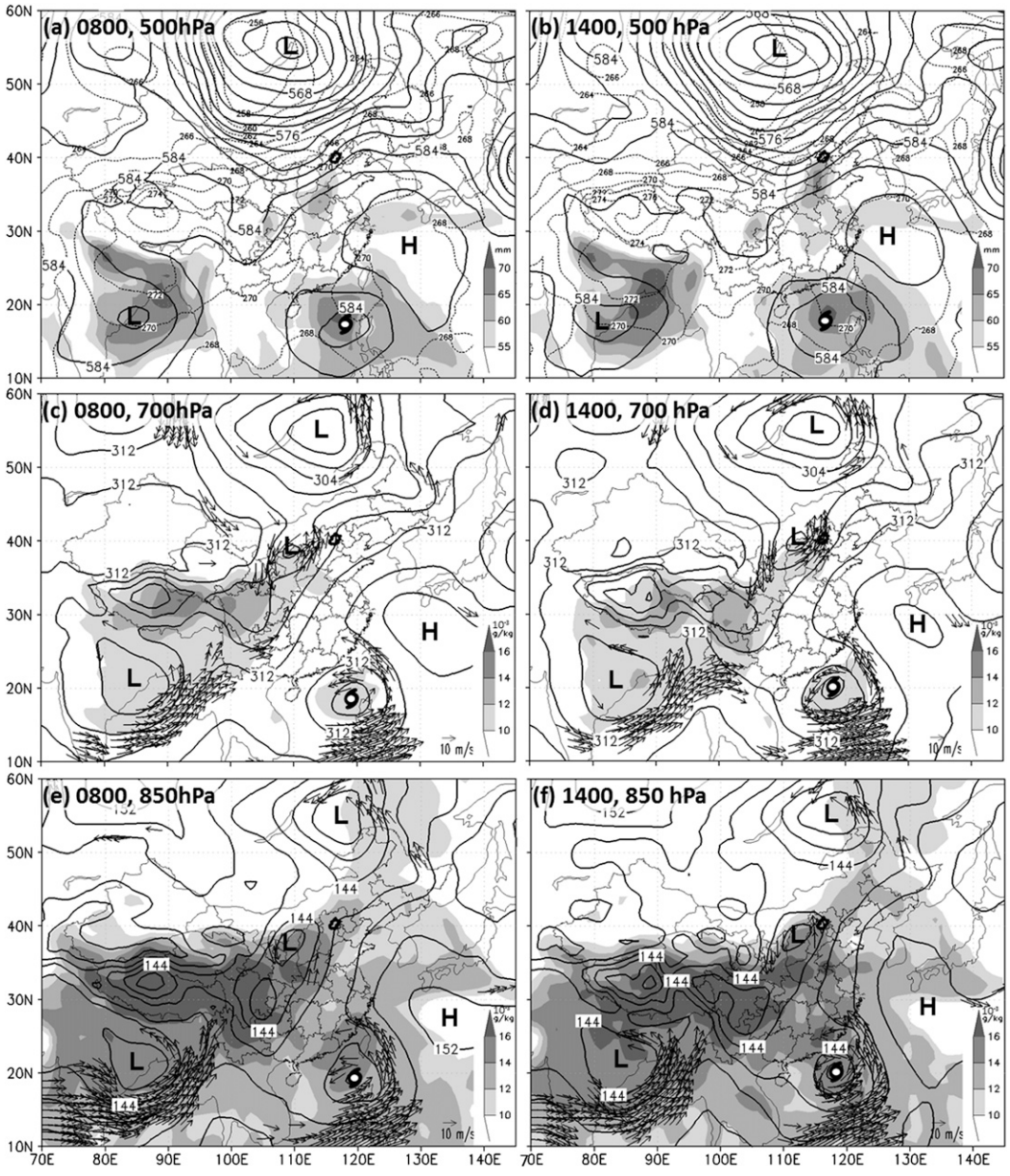

FIG. 17. (a) Geopotential height [black contours, 10 geopotential meters (gpm)] and temperature (K) at 500 hPa, and column-integrated precipitable water (mm) at 0800 LST 21 Jul 2012. (c) Geopotential height (black contours, 10 gpm), water vapor mixing ratio (10^{-3} g kg^{-1}), and wind vector stronger than 12 m s^{-1} at 700 hPa at 0800 LST. (e) As in (c), but for 850 hPa. (b),(d),(f) As in (a),(c),(e), but at 1400 LST. The metropolitan area of Beijing (near 39.9°N, 116.5°E) is highlighted by a heavy black curve. Letters H and L denote the high and low pressure centers, respectively. The typhoon symbol denotes the center of Typhoon Vincent.

located ~20 km west of where the tornado was generated (Fig. 18). The rawinsode at 1400 LST well represented the environment of the tornado since it was not only just ~20 km west of the tornado, but was also launched exactly at 1315 LST with the observations from 0 to 6 km AGL completed before the onset of tornado damage at ~1340 LST (Fig. 1b). The surface-based (SB) convective available potential energy (CAPE) with a virtual temperature correction increased from 1625 to 2737 J kg^{-1} (Figs. 18a,b) and became exactly the same as the most unstable (MU) CAPE, as indicated by a convective inhibition (CIN) of 0 J kg^{-1}. However, the high instability did not show up in the mean-layer-based (ML, 0–1 km AGL) CAPE (Table 1). The lowest 100-hPa layer AGL became much moister with a reduced SB lifting condensation level (LCL)

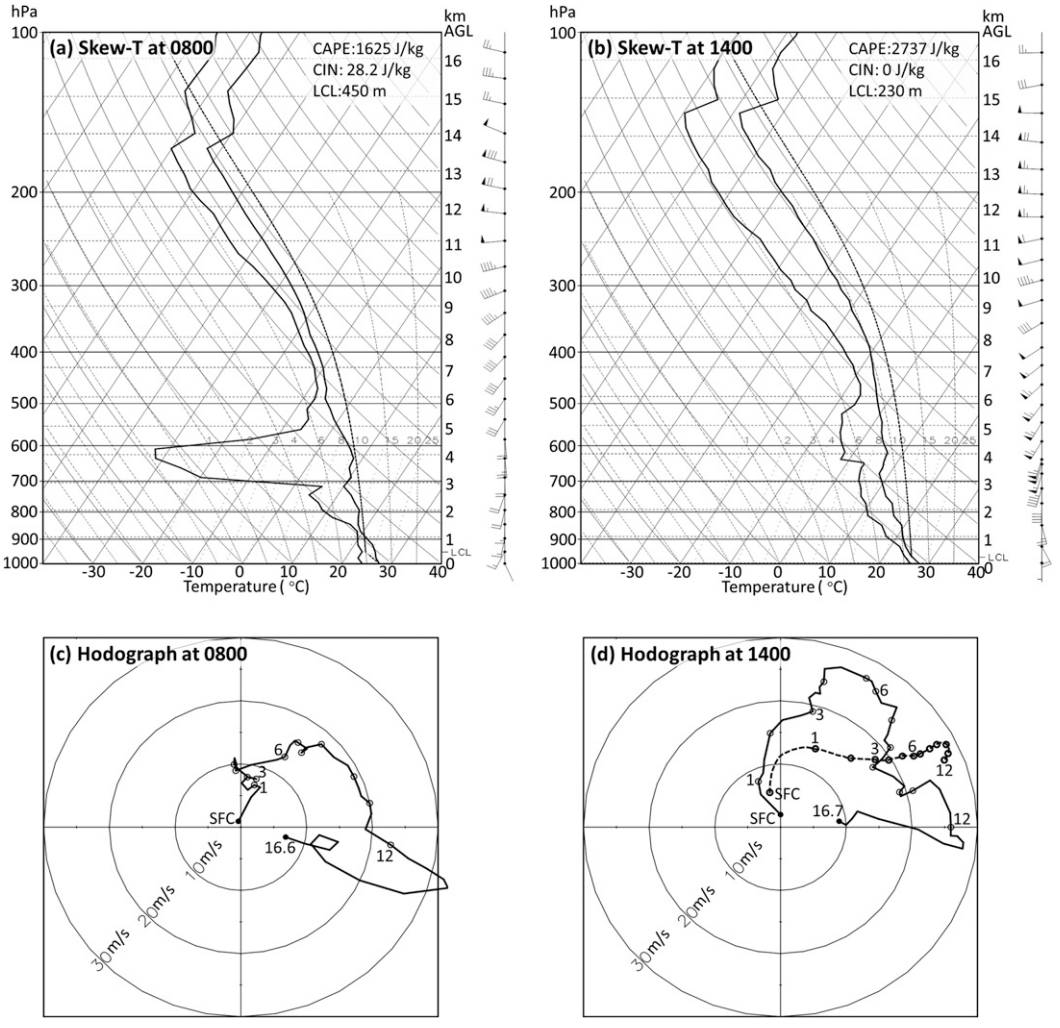

FIG. 18. (a),(b) Skew-*T* and (c),(d) hodograph diagrams of the Beijing rawinsonde at (left) 0800 and (right) 1400 LST 21 Jul 2012. Also shown on the right side of (a) and (b) are the horizontal wind barbs every other levels (full line, half line, and flag on the wind barb denote 2, 4, and 20 m s^{-1}, respectively). Surface-based CAPE, CIN, and LCL are given in the top-right corner of the Skew-*T* diagrams. The mean hodograph for the significantly tornadic environment adapted from Markowski et al. (2003) is plotted with dashed curve in (d) for reference. The small numbers in (c) and (d) denote the height (AGL) of different levels.

(Figs. 18a,b), which was regarded as a favorable condition for tornadic supercell formation (Craven and Brooks 2004). The MLCIN and MLLCL showed changes similar to those of SB cases.

The increase in low-level vertical shear is shown in the hodographs (Figs. 18c,d). The 0–6-km shear reached 23.4 m s^{-1} at 1400 LST (which was 9 m s^{-1} greater than that at 0800 LST) with a more apparent veering curvature. Compared to the mean hodograph of significantly tornadic supercells in the United States [Fig. 18d, dashed line, adapted from Markowski et al. (2003)], the Beijing case had a slightly smaller 0–1-km shear, and

TABLE 1. Environmental parameters of the supercell calculated with the rawinsonde of Beijing at 1400 UTC using a parcel lifted from the surface (SB) and a mean layer (ML, 0–1 km AGL).

	CAPE (J kg^{-1})	CIN (J kg^{-1})	LCL (km)	SHR1 (m s^{-1})	SHR6 (m s^{-1})	SRH1 (m^{-2} s^{-2})	SRH3 (m^{-2} s^{-2})	EHI1	EHI3	VGP	SCP	STP
SB	2737	0	0.23	7.1	23.4	73	262	1.25	4.48	0.397	18.9	2.7
ML	746	−0.2	0.71					0.34	1.22	0.207	5.2	0.54

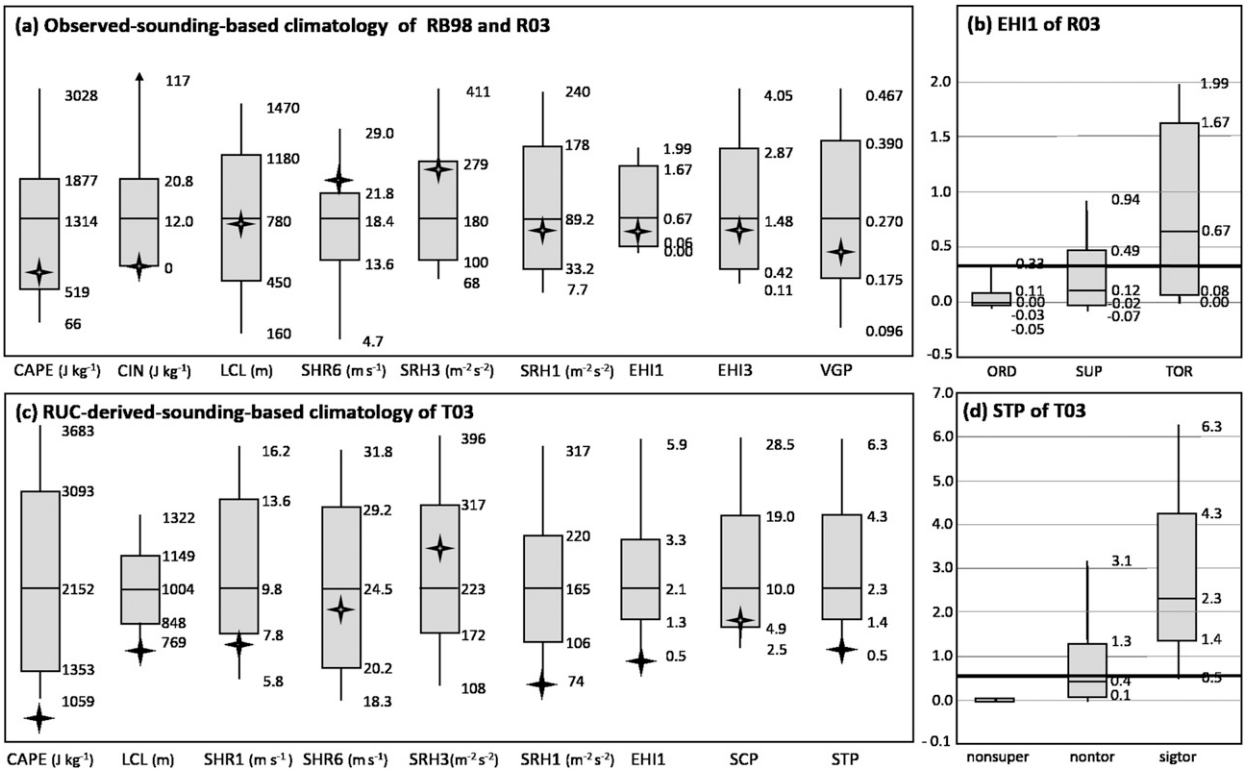

FIG. 19. Comparison of the parameters of the supercell environment calculated with the Beijing rawinsonde at 1400 LST using a parcel lifted from a mean layer (0–1 km AGL, black crosses) to (a) the climatology obtained for the significantly tornadic supercell category of RB98 (all parameters except for SRH1 and EHI1) and R03 (SRH1 and EHI1). (b) EHI1 (the long heavy line) is compared to the three categories of R03, including ORD, SUP, and TOR. (c) As in (a), but compared to the significantly tornadic supercell category of T03. (d) STP (the long heavy line) is compared to the three categories of T03, including nonsuper, nontor, and sigtor storms. The shaded box covers the 25th–75th percentiles, the whiskers extend to the 10th and 90th percentiles, and the median value is marked by the horizontal line within each shaded box.

similar 0–3- and 0–6-km shears with a more apparent veering curvature.

To determine how favorable the environment of this supercell was for tornadogenesis, we compared the sounding-derived parameters of this case at 1400 LST to the U.S. climatology. Rasmussen and Blanchard (1998, hereafter referred to as RB98) obtained a baseline climatology of observed-sounding-derived supercell and tornado forecast parameters using the U.S. soundings from the year 1992. They compiled statistics for three categories including nonsupercell thunderstorms or ordinary cells (ORD), supercells without significant tornadoes (SUP), and supercells with significant tornadoes (TOR). Significant tornadoes referred to those tornadoes of F2 and greater damage intensity. Since the Beijing tornado was rated EF3, the TOR category was used for comparison. To be comparable to RB98, mean-layer-based parameters using the lowest 1 km AGL with a virtual temperature correction were computed for the Beijing rawinsonde at 1400 LST (Table 1, Fig. 19a, crosses). Results showed that MLCAPE of the Beijing case was low, which was near the lower bound of the middle 50% of the U.S. climatology. The MLCIN was near zero, which was close to the median. Different from MLCAPE, the 0–6-km shear (SHR6) was high. It fell into the upper 25% of the U.S. climatology. The 0–3-km storm relative helicity (SRH3) and 0–1-km SRH (SRH1) were near the upper bound of the middle 50% and close to the median, respectively.

We then computed combination parameters, which have been regarded as being able to strongly discriminate between tornadic and nontornadic environments (e.g., RB98; Thompson et al. 2003, hereafter referred to as T03), using the same formula as in RB98. The results showed that both the 0–1-km energy-helicity index (EHI1; Rasmussen 2003, referred to as R03 hereafter) and the vorticity generation parameter (VGP; RB98) fell between 25% and 50% (Fig. 19a). Considering that EHI1 might be more effective in discriminating TOR from ORD and SUP (R03), the EHI1 of the Beijing case was compared to all three storm categories of R03 (Fig. 19b). The result showed that the value of the Beijing

case was at the top 10% of ORD and near the midpoint of the 25% above (below) the median of SUP (TOR). These results showed that the Beijing storm formed in an environment that was generally favorable for the formation of supercells, especially in terms of strong low-level shear. However, tornadogenesis was possible but significant tornadoes were not very likely. This environmental condition was manifested by only 1 of ~21 supercells observed that day (Yu 2012) becoming tornadic.

In addition to RB98, the supercell and tornado forecast parameters were also compared to another U.S. climatology produced by T03 and based on the proximate soundings derived from the Rapid Update Cycle (RUC) forecast model (Fig. 19c). T03 also used a virtual-temperature correction and mean-layer (the lowest 100 hPa, which is roughly the lowest 1 km) parcel. Comparing RB98 with T03 indicates that the environment for the formation of significantly tornadic supercells tends to have stronger instability (such as CAPE) and vertical wind shear (such as SHR6, SRH1, and SRH3) in the climatology based on the proximity soundings of RUC than that based on observed soundings. Within the context of the parameters of T03 for the significantly tornadic supercell category (which was equivalent to the TOR category in RB98), the environment of the Beijing tornado became generally less favorable (except for a more favorable LCL) for significant tornadogenesis than in RB98. We further compared the significant tornado parameter (STP), which is a composite parameter that can effectively discriminate significantly tornadic from nontornadic supercells (Thompson et al. 2003, 2012), to the three categories of T03 including nonsuper, nontor, and sigtor, which denote nonsupercell, nontornadic supercell, and significantly tornadic supercell storms, respectively. The value of the Beijing case (Fig. 19d, heavy line) was well above the 90th percentile of nonsuper while near the median of nontor and near the 10th percentile of sigtor. This result provided further evidence that the environment of the Beijing case was more favorable for the formation of nontornadic supercells rather than significantly tornadic supercells, which was consistent with the results obtained using the observed sounding-based 0–1-km EHI of R03.

5. Conclusions and discussion

Through a damage survey that had the most detailed information to date in China together with FNL, radar, and rawinsonde analyses, this work has clearly demonstrated that Zhangjiawan in Beijing, China, was hit by an EF3 tornado embedded within the mesocyclone of a supercell at ~1340–1400 LST on 21 July 2012. This was the first-ever documented tornado in Beijing. Two distinguishing signatures of a tornado were found based on the damage surveys: a narrow damage path and three places along the damage path that had an apparently convergent surface wind.

Our radar analyses show that this tornado was spawned in a strong mesocyclone of a supercell that developed at the southern end of a squall line. The period when the tornado caused severe damage and the period of the strong mesocyclone overlap. The intensification and expansion of the mesocyclone near the later stage of the tornado could be the reason for the sinusoidal tornado track likely because the tornado was embedded in the periphery of the mesocyclone.

Several tornado radar signatures were detected such as TVS, DRC, and TDS through S-band Doppler radar analyses. Relative to the mesocyclone, the TVS showed more coincidence with the wind damage in terms of their location, timing, and intensity variation. The TVS was detected first at 500 m ARL and rapidly developed upward and downward with time. The damage was the most severe when the TVS was detected near the ground at the lowest scan.

Two DRCs were detected, respectively, preceding the tornadogenesis and reintensification of the wind damage. The first DRC developed about 15 min before the onset of the wind damage. Similar to U.S. cases, jetlets accompanied by counterrotating vortices were observed to be associated with the DRCs. The cyclonic vortex associated with the first DRC was perfectly collocated with the TVS at 0.5° PPI and the tornado when the first sign of the damage was observed. The second DRC developed before the damage intensified after a short period of weakening. Furthermore, a TDS was detected during the later stages of the tornado. All these signatures provided further evidence for the occurrence of the tornado.

Compared to the observed-sounding-based U.S. climatology, the current reported tornadic supercell in Beijing formed in an environment with low MLCAPE, extremely low CIN, a close-to-median LCL, and low 0–1-km shear. A comparison across different convection categories of the combination parameters of 0–1-km EHI and STP, which are quite effective in discriminating tornadic and nontornadic supercells, indicated that this environment was quite favorable for the development of a nontornadic or weakly tornadic supercell rather than a significantly tornadic supercell.

With the above results in mind, we are interested in further examining the dynamics behind the evolution of various supercell and tornado signatures, especially the relationship among the tornado, TVS, DRC, and the parent mesocyclone. Cloud-resolving numerical simulations are

under way to examine the key environmental factors in the formation of the tornadic supercell, the origin of the rotation for the tornadogenesis, and the possible differences in the formation mechanism of the supercell and tornado in the monsoon climate regime from those in the United States and elsewhere, which will be presented in separate papers.

Acknowledgments. We thank Xiaoding Yu from China Meteorological Administration Training Center and Zuyu Tao from Peking University for their insightful comments. Special thanks also go to local government employees such as Xin Wang, Wensheng Qiao, and Youming Liang, and local residents in Zhangjiawan for sharing their memories about the tornado, and to all the photographers who shared their valuable pictures and videos of the tornado damage, especially Mingyuan Zhang. We also thank the Owner's Forum of GR2LevelX, from which we obtained much detailed information about GR2analyst software. This research was sponsored by the Ministry of Science and Technology of China with Grant 2013CB430104 and the Natural Science Foundation of China with Grants 41375048, 41075031, and 41175043.

REFERENCES

Agee, E. M., J. T. Snow, and P. R. Clare, 1976: Multiple vortex features in the tornado cyclone and the occurrence of tornado families. *Mon. Wea. Rev.,* **104,** 552–563, doi:10.1175/1520-0493(1976)104<0552:MVFITT>2.0.CO;2.

Alexander, C. R., and J. Wurman, 2005: The 30 May 1998 Spencer, South Dakota, storm. Part I: The structural evolution and environment of the tornadoes. *Mon. Wea. Rev.,* **133,** 72–97, doi:10.1175/MWR-2855.1.

Andra, D. L., 1997: The origin and evolution of the WSR-88D mesocyclone recognition nomogram. Preprints, *28th Conf. on Radar Meteorology,* Austin, TX, Amer. Meteor. Soc., 364–365.

Blanchard, D. O., 2013: A comparison of wind speed and forest damage associated with tornadoes in northern Arizona. *Wea. Forecasting,* **28,** 408–417, doi:10.1175/WAF-D-12-00046.1.

Bluestein, H. B., 1983: Surface meteorological observations in severe thunderstorms. Part II: Field experiments with TOTO. *J. Climate Appl. Meteor.,* **22,** 919–930, doi:10.1175/1520-0450(1983)022<0919:SMOIST>2.0.CO;2.

——, W. P. Unruh, D. C. Dowell, T. A. Hutchinson, T. M. Crawford, A. C. Wood, and H. Stein, 1997: Doppler radar analysis of the Northfield, Texas, tornado of 25 May 1994. *Mon. Wea. Rev.,* **125,** 212–230, doi:10.1175/1520-0493(1997)125<0212:DRAOTN>2.0.CO;2.

Brown, R. A., L. R. Lemon, and D. W. Burgess, 1978: Tornado detection by pulsed Doppler radar. *Mon. Wea. Rev.,* **106,** 29–38, doi:10.1175/1520-0493(1978)106<0029:TDBPDR>2.0.CO;2.

Bunkers, M. J., and M. A. Baxter, 2011: Radar tornadic debris signatures on 27 April 2011. *Electron. J. Oper. Meteor.,* **12** (7). 1–6. [Available online at http://www.nwas.org/ej/pdf/2011-ION1.pdf.]

Bunting, W. F., and B. E. Smith, 1993: A guide for conducting convective windstorm surveys. NOAA Tech. Memo. NWS SR146, Scientific Services Division, NWS Southern Region, Fort Worth, TX, 44 pp.

Burgess, D. W., L. R. Lemon, and R. A. Brown, 1975a: Evolution of a tornado signature and parent circulation as revealed by single Doppler radar. Preprints, *16th Conf. on Radar Meteorology,* Houston, TX, Amer. Meteor. Soc., 99–106.

——, ——, and ——, 1975b: Tornado characteristics revealed by Doppler radar. *Geophys. Res. Lett.,* **2,** 183–184, doi:10.1029/GL002i005p00183.

Byko, Z., P. Markowski, Y. Richardson, J. Wurman, and E. Adlerman, 2009: Descending reflectivity cores in supercell thunderstorms observed by mobile radars and in a high-resolution numerical simulation. *Wea. Forecasting,* **24,** 155–186, doi:10.1175/2008WAF2222116.1.

Chen, Y., and Coauthors, 2012: Analysis and thinking on the extremes of the 21 July 2012 torrential rain in Beijing. Part I: Observation and thinking (in Chinese with English abstract). *Meteor. Monogr.,* **38,** 1255–1266.

Craven, J. P., and H. E. Brooks, 2004: Baseline climatology of sounding derived parameters associated with deep, moist convection. *Natl. Wea. Dig.,* **28,** 13–24.

Davies-Jones, R. P., D. W. Burgess, L. R. Lemon, and D. Purcell, 1978: Interpretation of surface marks and debris patterns from the 24 May 1973 Union City, Oklahoma tornado. *Mon. Wea. Rev.,* **106,** 12–21, doi:10.1175/1520-0493(1978)106<0012:IOSMAD>2.0.CO;2.

Donaldson, R. J., 1970: Vortex signature recognition by a Doppler radar. *J. Appl. Meteor.,* **9,** 661–670, doi:10.1175/1520-0450(1970)009<0661:VSRBAD>2.0.CO;2.

Doswell, C. A., III, 2003: A guide to F-scale damage assessment. NOAA/NWS, 94 pp. [Available online at http://www.wdtb.noaa.gov/courses/ef-scale/lesson2/FinalNWSF-scaleAssessmentGuide.pdf.]

Fang, L., J. Ji, G. Tao, C. Zhou, and K. Wang, 2009: Weather analysis and grade determination of a tornado occurring in a single super-storm (in Chinese with English abstract). *J. Nat. Disasters,* **2,** 167–172.

Frelich, L. E., and E. J. Ostuno, 2012: Estimating wind speeds of convective storms from tree damage. *Electron. J. Severe Storms Meteor.,* **7** (9). [Available online at http://www.ejssm.org/ojs/index.php/ejssm/article/viewFile/111/87.]

French, M., and H. Bluestein, I. PopStefanija, C. A. Baldi, and R. T. Bluth, 2013: Reexamining the vertical development of tornadic vortex signatures in supercells. *Mon. Wea. Rev.,* **141,** 4576–4601, doi:10.1175/MWR-D-12-00315.1.

Fujita, T. T., 1971a: Proposed characterization of tornadoes and hurricanes by area and intensity. SMRP Research Paper 91, University of Chicago, 42 pp.

——, 1971b: Proposed mechanism of suction spots accompanied by tornadoes. Preprints, *Seventh Conf. on Severe Local Storms,* Kansas City, MO, Amer. Meteor. Soc., 208–213.

——, 1974: Jumbo tornado outbreak of 3 April 1974. *Weatherwise,* **27,** 116–126, doi:10.1080/00431672.1974.9931693.

——, 1981: Tornadoes and downbursts in the context of generalized planetary scales. *J. Atmos. Sci.,* **38,** 1511–1534, doi:10.1175/1520-0469(1981)038<1511:TADITC>2.0.CO;2.

Glickman, T., Ed., 2000: *Glossary of Meteorology.* 2nd ed. Amer. Meteor. Soc., 855 pp. [Available online at http://glossary.ametsoc.org.]

Kennedy, A., J. M. Straka, and E. N. Rasmussen, 2007: A statistical study of the association of DRCs with supercells and tornadoes. *Wea. Forecasting,* **22,** 1191–1199, doi:10.1175/2007WAF2006095.1.

Lee, R., and A. White, 1998: Improvement of the WSR-88D mesocyclone algorithm. *Wea. Forecasting,* **13,** 341–351, doi:10.1175/1520-0434(1998)013<0341:IOTWMA>2.0.CO;2.

Lin, Z., 1995: Damage survey on "6.9" tornadoes in Nanhai & Guangzhou (in Chinese). *Guangdong Meteor.,* **7,** 36–38.

Markowski, P., and Y. Richardson, 2010: *Mesoscale Meteorology in Midlatitudes.* Wiley-Blackwell, 424 pp.

——, C. Hannon, J. Frame, E. Lancaster, A. Pietrycha, R. Edwards, and R. Thompson, 2003: Characteristics of vertical wind profiles near supercells obtained from the Rapid Update Cycle. *Wea. Forecasting,* **18,** 1262–1272, doi:10.1175/1520-0434(2003)018<1262:COVWPN>2.0.CO;2.

——, and Coauthors, 2012a: The pretornadic phase of the Goshen County, Wyoming, supercell of 5 June 2009 intercepted by VORTEX2. Part I: Evolution of kinematic and surface thermodynamic fields. *Mon. Wea. Rev.,* **140,** 2887–2915, doi:10.1175/MWR-D-11-00336.1.

——, and Coauthors, 2012b: The pretornadic phase of the Goshen County, Wyoming, supercell of 5 June 2009 intercepted by VORTEX2. Part II: Intensification of low-level rotation. *Mon. Wea. Rev.,* **140,** 2916–2938, doi:10.1175/MWR-D-11-00337.1.

Marshall, T. P., 2002: Tornado damage survey at Moore, Oklahoma. *Wea. Forecasting,* **17,** 582–598, doi:10.1175/1520-0434(2002)017<0582:TDSAMO>2.0.CO;2.

Meng, Z., D. Yan, and Y. Zhang, 2013: General features of squall lines in east China. *Mon. Wea. Rev.,* **141,** 1629–1647, doi:10.1175/MWR-D-12-00208.1.

Mou, Z., C. Zhang, and X. Pan, 2001: A damage survey of the tornado first captured by meteorological instrument in Zhejiang China (in Chinese with English abstract). *J. Zhejiang Meteor.,* **22,** 41–43.

Rasmussen, E. N., 2003: Refined supercell and tornado forecast parameters. *Wea. Forecasting,* **18,** 530–535, doi:10.1175/1520-0434(2003)18<530:RSATFP>2.0.CO;2.

——, and D. O. Blanchard, 1998: A baseline climatology of sounding-derived supercell and tornado forecast parameters. *Wea. Forecasting,* **13,** 1148–1164, doi:10.1175/1520-0434(1998)013<1148:ABCOSD>2.0.CO;2.

——, J. M. Straka, M. S. Gilmore, and R. Davies-Jones, 2006: A preliminary survey of rear-flank descending reflectivity cores in supercell storms. *Wea. Forecasting,* **21,** 923–938, doi:10.1175/WAF962.1.

Ryzhkov, A., T. J. Schuur, D. W. Burgess, and D. S. Zrnić, 2005: Polarimetric tornado detection. *J. Appl. Meteor.,* **44,** 557–570, doi:10.1175/JAM2235.1.

Smith, B. T., R. L. Thompson, J. S. Grams, C. Broyles, and H. E. Brooks, 2012: Convective modes for significant severe thunderstorms in the contiguous United States. Part I: Storm classification and climatology. *Wea. Forecasting,* **27,** 1114–1135, doi:10.1175/WAF-D-11-00115.1.

Smith, T. M., and K. L. Elmore, 2004: The use of radial velocity derivatives to diagnose rotation and divergence. Preprints, *11th Conf. on Aviation, Range and Aerospace,* Hyannis, MA, Amer. Meteor. Soc., P5.6. [Available online at http://ams.confex.com/ams/pdfpapers/81827.pdf.]

Speheger, D. A., C. A. Doswell III, and G. J. Stumpf, 2002: The tornadoes of 3 May 1999: Event verification in central Oklahoma and related issues. *Wea. Forecasting,* **17,** 362–381, doi:10.1175/1520-0434(2002)017<0362:TTOMEV>2.0.CO;2.

Stumpf, G. J., A. Witt, E. D. Mitchell, P. L. Spencer, J. T. Johnson, M. D. Eilts, K. W. Thomas, and D. W. Burgess, 1998: The National Severe Storms Laboratory Mesocyclone Detection Algorithm for the WSR-88D. *Wea. Forecasting,* **13,** 304–326, doi:10.1175/1520-0434(1998)013<0304:TNSSLM>2.0.CO;2.

Tang, X., and Y. Liao, 2007: An analysis of a tornado in Yongzhou, Hunan Province (in Chinese with English abstract). *Meteor. Monogr.,* **33,** 23–28.

Thompson, R. L., R. Edwards, J. A. Hart, K. L. Elmore, and P. Markowski, 2003: Close proximity soundings within supercell environments obtained from the Rapid Update Cycle. *Wea. Forecasting,* **18,** 1243–1261, doi:10.1175/1520-0434(2003)018<1243:CPSWSE>2.0.CO;2.

——, B. T. Smith, J. S. Grams, A. R. Dean, and C. Broyles, 2012: Convective modes for significant severe thunderstorms in the contiguous United States. Part II: Supercell and QLCS tornado environments. *Wea. Forecasting,* **27,** 1136–1154, doi:10.1175/WAF-D-11-00116.1.

Trapp, R. J., E. D. Mitchell, G. A. Tipton, D. W. Effertz, A. I. Watson, D. L. Andra, and M. A. Magsig, 1999: Descending and nondescending tornadic vortex signatures detected by WSR-88Ds. *Wea. Forecasting,* **14,** 625–639, doi:10.1175/1520-0434(1999)014<0625:DANTVS>2.0.CO;2.

Wakimoto, R. M., H. V. Murphey, D. C. Dowell, and H. B. Bluestein, 2003: The Kellerville tornado during VORTEX: Damage survey and Doppler radar analyses. *Mon. Wea. Rev.,* **131,** 2197–2221, doi:10.1175/1520-0493(2003)131<2197:TKTDVD>2.0.CO;2.

WDTB, cited 2013a: Supercell velocity signatures: Lesson 9. NOAA/Warning Decision Training Branch. [Available online at http://www.wdtb.noaa.gov/courses/dloc/topic7/lesson9/player.html.]

——, cited 2013b: Supercell velocity signatures: Lesson 12. NOAA/Warning Decision Training Branch. [Available online at http://www.wdtb.noaa.gov/courses/dloc/topic7/lesson12/player.html].

WSEC, 2006: A recommendation for an enhanced Fujita scale (EF-scale). Wind Science and Engineering Center Rep., Texas Tech University, Lubbock, TX, 95 pp. [Available online at http://www.spc.noaa.gov/faq/tornado/ef-ttu.pdf.]

Yang, Q., C. Chen, and M. Wu, 1978: A damage survey and preliminary analysis on a tornado (in Chinese). *Meteor. Monogr.,* **4,** 16–17.

Yu, X., 2012: Investigation of Beijing extreme flooding event on 21 July 2012 (in Chinese with English abstract). *Meteor. Monogr.,* **38,** 1313–1329.

Zhao, Y., 1995: *Studies on Meso to Small Scale Weathers* (in Chinese). Meteorological Press, 75 pp.

Zheng, F., 2009: A strong tornado in the outer-region of the super typhoon "Sepat"in 2007 (in Chinese with English abstract). *Chin. Agric. Sci. Bull.,* **25** (12), 283–286.

Zhu, X., and J. Zhu, 2004: New generation weather radar network in China (in Chinese with English abstract). *Mater. Sci. Technol.,* **32,** 255–258.

Zrnić, D., and M. Istok, 1980: Wind speeds in two tornadic storms and a tornado deduced from Doppler spectra. *J. Appl. Meteor.,* **19,** 1405–1415, doi:10.1175/1520-0450(1980)019<1405:WSITTS>2.0.CO;2.